

# Interactive Scene Authoring with Specialized Generative Primitives

CLÉMENT JAMBON, ETH Zurich, Switzerland  
 CHANGWOON CHOI, Seoul National University, South Korea  
 DONGSU ZHANG, Seoul National University, South Korea  
 OLGA SORKINE-HORNUNG, ETH Zurich, Switzerland  
 YOUNG MIN KIM, Seoul National University, South Korea

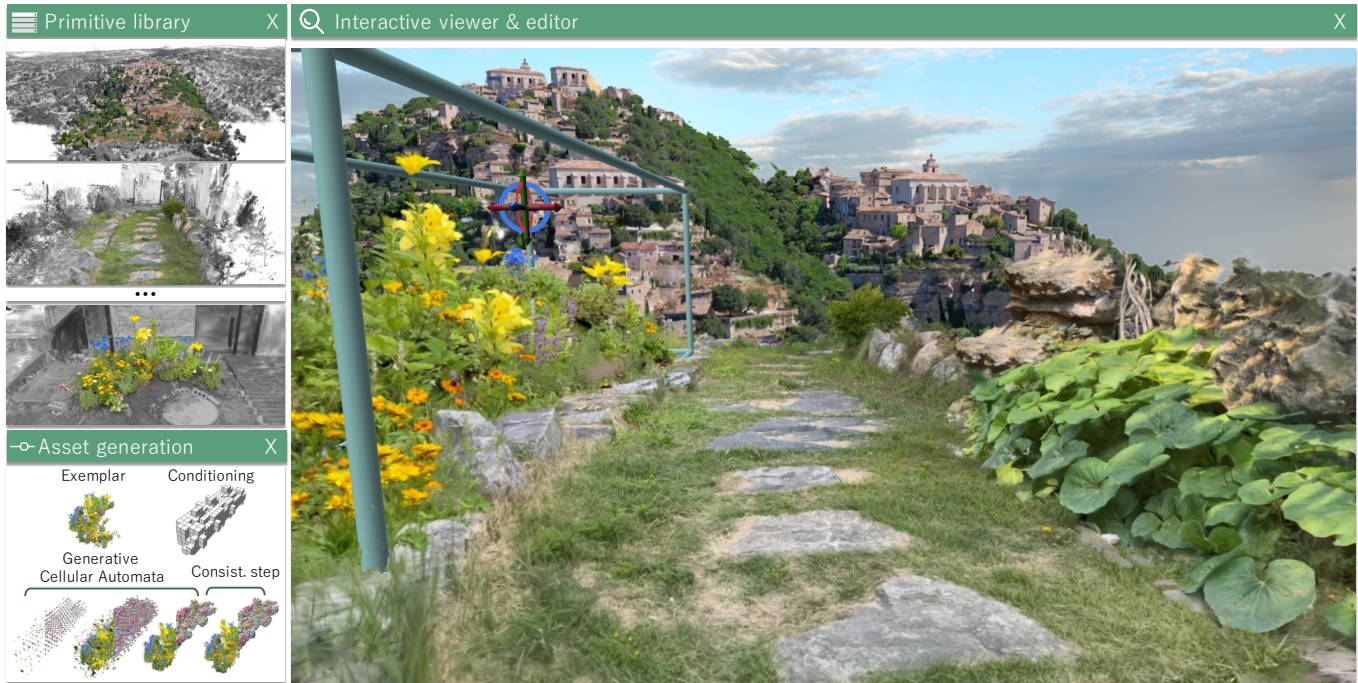


Fig. 1. We propose an interactive framework to author 3D scenes using “Specialized Generative Primitives”, a lightweight and controllable generative model. Casual video inputs are turned into a high-quality 3D representation using 3D Gaussian splats. Within our editor and with guidance from semantic segments, users extract regions they wish to build a primitive from (colored region in the “Primitive library” window). After only 10 minutes of training, each primitive is used to author assets independently using voxelized coarse conditioning inputs (“Asset generation” window). Generation follows two steps: (a) sampling using Generative Cellular Automata, (b) a patch consistency step. Generated results can be further composited into a complex scene within a fully interactive viewer (right-most window). In this scene, every asset was generated using our primitives with the exception of the environment map. We detail this composition in the supplemental video.

Generating high-quality 3D digital assets often requires expert knowledge of complex design tools. We introduce Specialized Generative Primitives, a generative framework that allows non-expert users to author high-quality 3D scenes in a seamless, lightweight, and controllable manner. Each primitive is an efficient generative model that captures the distribution of a single exemplar from the real world. With our framework, users capture a video of an environment, which we turn into a high-quality and explicit appearance model thanks to 3D Gaussian Splatting. Users then select regions of interest guided by semantically-aware features. To create a generative primitive, we adapt Generative Cellular Automata to single-exemplar training and

controllable generation. We decouple the generative task from the appearance model by operating on sparse voxels and we recover a high-quality output with a subsequent sparse patch consistency step. Each primitive can be trained within 10 minutes and used to author new scenes interactively in a fully compositional manner. We showcase interactive sessions where various primitives are extracted from real-world scenes and controlled to create 3D assets and scenes in a few minutes. We also demonstrate additional capabilities of our primitives: handling various 3D representations to control generation, transferring appearances, and editing geometries.

Authors’ Contact Information: Clément Jambon, ETH Zurich, Zurich, Switzerland, cjambon@student.ethz.ch; Changwoon Choi, Seoul National University, Seoul, South Korea, changwoon.choi00@gmail.com; Dongsu Zhang, Seoul National University, Seoul, South Korea, 96lives@gmail.com; Olga Sorkine-Hornung, ETH Zurich, Zurich, Switzerland, sorkine@inf.ethz.ch; Young Min Kim, Seoul National University, Seoul, South Korea, youngmin.kim@snu.ac.kr.

CCS Concepts: • **Computing methodologies** → **Graphics systems and interfaces**; **Artificial intelligence**.

Additional Key Words and Phrases: Interactive Tool, Generative Cellular Automata, 3D Gaussian Splatting, Scene Authoring, Patch-based Optimization

## 1 INTRODUCTION

Sophisticated tools for designing 3D content require expertise, which hinders the general public from experiencing interactive and intuitive control for 3D creation. Neural Radiance Fields (NeRF) [Mildenhall et al. 2021] have revolutionized the task of 3D scene reconstruction and novel view synthesis. Thanks to significant advances in terms of speed [Müller et al. 2022], improved sampling techniques [Barron et al. 2023], and open frameworks [Tancik et al. 2023], they have given everyone the possibility to casually capture complex scenes within minutes and at unprecedented levels of realism. However, *interactive* and *creative* authoring beyond simple modifications of static scenes is still challenging. On the other hand, recent advancements in generative frameworks [Hong et al. 2023; Poole et al. 2022; Ren et al. 2023] trained from large-scale images or foundation text-to-image priors [Rombach et al. 2022] and 3D datasets [Deitke et al. 2023] have enabled impressive creations. However, they are limited to high-level control and modeling distributions contained in their training dataset [Dong et al. 2024; Po and Wetzstein 2023; Wang et al. 2024b], thus precluding fine-level feedback from users. Additionally, they are relatively slow due to the sampling paradigms they rely on (e.g., diffusion).

We instead propose to take a radically different route: “What if we could directly turn any casually captured NeRF into a generative primitive and gather a collection of such specialized primitives that we could use individually and recompose at will?”. We build on the observation that most content-authoring tools from raster and vector graphics editors [Adobe Inc. 2024a,b] to 3D and VR modeling tools [Adobe Inc. 2024c; Media Molecule 2020; Oculus VR 2016] usually rely on a set of primitives and brushes that artists collect and learn to master over time. We transport this idea in a literal way to NeRF, or more precisely 3D Gaussian Splatting (3DGS) [Kerbl et al. 2023], by turning casually-captured scenes into *Specialized Generative Primitives*. These primitives can be extracted intuitively from neural 3D representations, trained within a moderate amount of time, and used in real-time in a controllable and compositional manner to author realistic 3D scenes.

To propose high-quality real-time authoring sessions, we use 3DGS [Kerbl et al. 2023] as our appearance model. This enables users to start freely from a video and turn it into an explicit 3D representation that can be further manipulated and converted into a *specialized* generative model. Without external priors, building a generative model over a complex and unstructured field of 3D Gaussians is an extremely complicated task. We thus decouple the task of learning a generative prior from modeling the actual appearance. To do so, the initial set of 3D Gaussians is mapped to a sparse voxel hierarchy augmented by semantically-aware features that we distill from foundation models, namely DINO features [Caron et al. 2021]. To recover high-quality outputs, inspired by patch-based synthesis algorithms [Barnes et al. 2009; Barnes and Zhang 2017], we introduce a *sparse* and thus efficient patch consistency step over the sparse volume of voxels.

Previous works [Li et al. 2023; Wang et al. 2022b] rely on *dense* hierarchical patch-based synthesis as a generative model over radiance fields. This comes at the cost of efficiency, lack of explicit control, and struggles to reconstruct highly semantic or relatively

structured objects because it only relies on multi-scale patch statistics. We instead propose to leverage *Generative Cellular Automata* (GCA) [Zhang et al. 2021, 2022], a lightweight generative model that operates directly on sparse 3D voxels. As a contribution, we extend it to fast single-exemplar training (less than 10 minutes), modeling appearance, and controllable generation conditioned on a coarser level of the above-mentioned voxel hierarchy. GCA allows for fast generation (0.5 to 2 seconds) which, combined with real-time rendering of 3D Gaussians, enables seamless and iterative authoring sessions.

As we seek to demonstrate an end-to-end creative solution, we embed *every* part of this pipeline into a self-contained and intuitive editor, from the selection and preparation of primitives to compositional editing. To do so, we introduce a suggestive and refinable selection system, where we reuse the previously mentioned DINO features. As no external priors are used, our primitives only produce consistent results close to the original structure of the exemplar. To nudge users to do so, we propose “exemplar brushes” that can be built directly from the exemplar and resampled during authoring.

We implement our method as a fully interactive authoring framework that we will release with this paper. To showcase it, we provide a dataset of “Specialized Generative Primitives” built from scenes casually captured with smartphones or drones. All the scenes used in this paper are *real-world* scenes without any exception. We show how our primitives can be used in different combinations and for various applications. More concretely, our approach can model distributions at any scale: individual objects (e.g., a single flower), human-scale regions (e.g., a garden, a pond), and large-scale scenes (e.g., “miniature” city blocks, an island). With appropriate guidance, our primitives can be applied to unstructured and moderately structured 3D distributions. We also show that our method naturally applies to appearance transfer across shapes and primitives. Thanks to our lightweight and decoupled generative model, we show that users can instantly generate many diverse variants. This provides a seamless interface to author content iteratively. We invite readers to check our supplementary video. Finally, due to the explicitness of 3D Gaussians, our primitives can be composed into complex real scenes and further exported and shared on edge devices, such as browsers and smartphones.

## 2 RELATED WORKS

Our generative primitives adapt various 3D representations from state-of-the-art works to provide easy-to-control, high-quality 3D scene authoring with coarse, but intuitive and explicit user control. We first discuss recent advances in neural scene reconstructions and leveraging additional signals in 3D in Section 2.1. We then touch upon various 3D generation pipelines that allow user control in Section 2.2. Lastly, Section 2.3 covers related works on intuitive content authoring and exemplar-based works that share a similar goal to ours.

### 2.1 High-quality Appearance Models & Semantic Features

*NeRF-like appearance models.* Since their introduction, Neural Radiance Fields (NeRFs) [Mildenhall et al. 2021] have greatly benefited 3D content creation. This can be explained in many ways: they

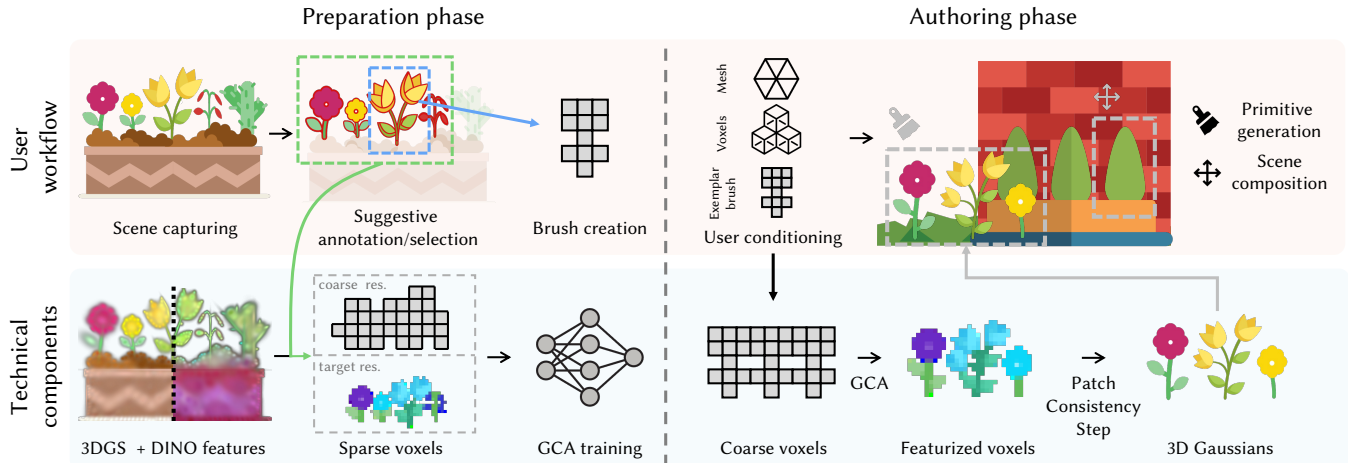


Fig. 2. Overview of the user workflow (first row) and the underlying technical components (second row). *Preparation phase.* A user captures a 3D scene that is reconstructed as 3D Gaussians augmented with DINO features. With the guidance of these features, the user can extract the region of interest as well as optional “exemplar brushes”. A hierarchy of sparse voxels is built from the former and used to train a “specialized primitive” using GCA at a target resolution conditioned on a given coarse resolution. *Authoring phase.* The user can author content with this primitive through multiple modalities (“exemplar brush”, mesh, or direct voxel editing) that are converted into coarse voxels. The output of each primitive can be freely composited with other primitives or static 3D Gaussian regions. Under the hood, each primitive samples a featurized grid of voxels at the target resolution from the coarse conditioning voxels through GCA. These voxels are then remapped to the set of 3D Gaussians in the exemplar with our sparse patch consistency step.

provide high-quality appearance models [Barron et al. 2023; Wang et al. 2023], efficient training [Fridovich-Keil et al. 2022; Müller et al. 2022], and direct deployment on edge devices at real-time framerates [Chen et al. 2023c; Duckworth et al. 2023]. Most importantly, they come with great ease of capture: they can be trained directly from casual videos captured with hand-held devices. More recently, 3DGS [Kerbl et al. 2023] has strengthened these arguments by switching the paradigm from volume rendering to differentiable rasterization through alpha-compositing of 3D Gaussians.

*Feature fields & semantically-aware grouping.* Volume rendering and alpha-compositing can be extended to distill 2D feature maps as *feature fields* [Kobayashi et al. 2022; Tschernetzki et al. 2022]. This has been used to leverage other modalities such as text [Radford et al. 2021] through language embedded fields [Kerr et al. 2023] or to perform advanced (hierarchical) grouping and scene understanding of 3D scenes [Bhalgat et al. 2024; Kim et al. 2024; Ye et al. 2023]. Inspired by these methods, we also train a feature field of 3D Gaussians with DINO features [Caron et al. 2021; Oquab et al. 2023]. In our work, these features serve a dual purpose: (a) when quantized, they provide 3D semantic masks that we use as a suggestive selection mechanism, (b) they provide additional semantic information that we use to train our generative model from a single exemplar. However, contrary to recent works that leverage these features in their full dimensionality [Zhou et al. 2023], we seek a solution amenable to interactive use, and we thus reduce their dimension through PCA on a per-primitive basis.

## 2.2 Controllable Generation & Authoring

*Controllable 3D generation.* Controllable 3D generation methods have recently greatly benefited from advances in 2D foundation

models [Rombach et al. 2022] and large-scale 3D datasets [Deitke et al. 2023]. For instance, starting from text prompts, some works leverage 2D diffusion priors through *Score Distillation Sampling* (SDS) [Lin et al. 2023; Poole et al. 2022]. Major limitations of such methods are the expensive optimization process, the limited control and biases from text-to-image priors, and the focus on object-centric representations. More recent methods have addressed some of these limitations. Optimization has been amortized [Xie et al. 2024a], or feed-forward architectures [Szymanowicz et al. 2023] have been proposed. Additional control can be provided in the form of coarse shape inputs [Dong et al. 2024], sketches [Chen et al. 2023d; Liu et al. 2024], or 3D exemplars through fine-tuning [Wang et al. 2024b]. Scene generation through layout control has also been proposed [Wu et al. 2024] but requires extensive procedural data generation and is thus limited by the training distribution.

*Editing of existing 3D object & scenes.* Previous works have proposed to edit NeRFs through explicit deformations of the radiance volume [Jambon et al. 2023; Yuan et al. 2022] or following 3D scene flows [Tang et al. 2024], using gradient propagation to stitch parts [Gong et al. 2023], or editing color or style through image-space losses [Wang et al. 2024a; Zhang et al. 2024]. More recently, 3DGS has made these edits even more straightforward. However, such edits are heavily restricted to the initial structure of the scene and often require cumbersome preparation stages. By combining 3DGS with an intuitive interface and the guidance of DINO features, we propose a seamless authoring workflow. To extrapolate beyond the distribution of the captured scene, controllable 3D generation techniques have been adapted to 3D scene editing [Chen et al. 2023a; Zhuang et al. 2023] or mesh sculpting [Gao et al. 2023a].

Image-to-image priors have been used to update NeRFs progressively [Dihlmann et al. 2024; Haque et al. 2023]. Even when providing other forms of control (e.g., sketches [Mikaeili et al. 2023]), these methods often rely strongly on text as a conditioning modality.

### 2.3 Intuitive Authoring & Exemplar-based Approaches

*Progressive & intuitive authoring workflows.* We seek a more straightforward form of control building on the intuition that people tend to “follow a coarse-to-fine drawing strategy, first outlining the shape using longer strokes and then adding detail at the end of the sketching process” [Eitz et al. 2012]. Progressive and guided authoring strategies have been explored extensively in computer graphics [Fernquist et al. 2011; Iarussi et al. 2013; Sarukkai et al. 2024b]. Often, the crucial point is the granularity of control provided to the user, as this implies a trade-off between expressivity and ease of use. In 2D, this can be subsets of the original image [Mu et al. 2024], sketches and masks [Zhang et al. 2023], or a collage of exemplar layers [Sarukkai et al. 2024a]. For 3D tasks, this can be 2D curves that are lifted in 3D [Dvorožňák et al. 2020; Zheng et al. 2024], voxels [Hao et al. 2021], or even text through nested prompts [Cheng et al. 2023]. We choose 3D voxels because, despite their simplicity, they provide intuitive control that can lead to surprisingly complex creations [Mojang Studios 2011]. More importantly, they are adapted to efficiency, particularly for the generative model we introduce in Section 5. Our work is also related to the task of shape and appearance detailization [Chen et al. 2023b, 2021; Li et al. 2024]. However, we seek to stay close to an input scene to provide explicit control on the distribution that is produced by our model.

*Exemplar-based methods.* This naturally leads to exemplar-based methods [Diamanti et al. 2015]. To learn the generative prior and amortize the cost of generating shapes, we draw inspiration from recent works that operate over a single exemplar. These approaches, both in 2D [Nikankin et al. 2022; Shaham et al. 2019; Wang et al. 2022a] and in 3D [Wu et al. 2023; Wu and Zheng 2022], rely on random augmentations and limited receptive fields to yield relative generalization. Contrary to concurrent works [Wu et al. 2023; Wu and Zheng 2022], we do not learn a per-exemplar latent space (e.g., triplane) as we seek a solution that is fast enough for real-time rendering and explicit enough for direct manipulation and control. We achieve this with the guidance of additional features (i.e., DINO) and using a probabilistic generative model operating directly on sparse 3D voxels, namely *Generative Cellular Automata* (GCA) [Zhang et al. 2021, 2022]. Another approach is also inspired by Cellular Automata, namely *Neural Cellular Automata* (NCA) [Mordvintsev et al. 2020]. It has been used for generating 2D textures [Niklasson et al. 2021] and UV-mapped textures on meshes [Pajouheshgar et al. 2023] in a data-efficient manner. However, NCA is based on a different paradigm inspired by biology.

Many exemplar-based methods rely on patch-based synthesis or optimization [Barnes and Zhang 2017; Jung et al. 2024]. A seminal work in this direction is the *PatchMatch* algorithm [Barnes et al. 2009]. Patch-based synthesis algorithms alternate repetitively between two stages: (a) an exact or approximate matching algorithm pairs a patch of the target representation to a patch in the exemplar, (b) patches from the exemplar are aggregated to produce a

new target representation. This process is repeated multiple times, usually until convergence is reached. Initially introduced in 2D, this technique was recently repurposed as a 3D “generative model” for natural scenes [Li et al. 2023]. This work uses a hierarchical coarse-to-fine approach to synthesize a radiance volume. However, relying on patch-based statistics in a unidirectional way (i.e., top-down [Wang et al. 2022b]) fails to reproduce highly semantic or structural information. Moreover, it operates densely over the radiance volume. In our work, we instead introduce a patch-based *consistency* step as the final stage of generation only. To do so, we propose a *sparse* 3D formulation directly applicable to our sparse voxelized representation.

## 3 OVERVIEW

Our pipeline is illustrated in Figure 2. The first row summarizes the user workflow, highlighting the user-friendly interface of our 3D authoring tool. We further present user creations in Section 6. The second row in Figure 2 contains the technical components that our system relies on. We provide detailed descriptions in Sections 4 and 5. We ablate the proposed components to analyze their effectiveness and limitations in Section 7.

### 3.1 User Workflow

At a high level, the user first extracts primitives from casual inputs (preparation phase) and uses them to author the scene (authoring phase).

- (1) *Scene capture.* Users start by capturing a video with a commodity device, for example, a smartphone. The scene should contain the object or region from which the user wants to build a generative primitive.
- (2) *Region selection.* After only a few minutes, our system provides a 3D representation of the captured content. Then, users can select the object or region within the scene guided by suggestive segments from the interface. Users can adjust the granularity of segments on the fly. This selection defines the *Specialized Generative Primitive*.
- (3) *Brush creation.* Additionally, users can further refine these annotations and extract coarse subsets of the geometry using the same mechanism. The latter will be used as *exemplar brushes* to compose a novel scene.
- (4) *Primitive training & generation.* After 10 minutes of training, users can use the corresponding *Specialized Generative Primitive* and their *exemplar brushes* to produce new variations of the initial exemplar.
- (5) *Scene authoring.* Users are now free to interactively compose the primitives to build a scene with a high-quality appearance, without requiring special expertise. Note that it is also possible to mix and match, as we show in Section 6: one can use brushes from other scenes, external meshes, or even a manually designed set of voxels of a shape – any coarse geometry can serve as a conditioning signal to the system.

The user, therefore, has complete control of the pipeline, from capturing the ingredients for primitives to scene composition. Our GUI provides an intuitive interface to support exploration.

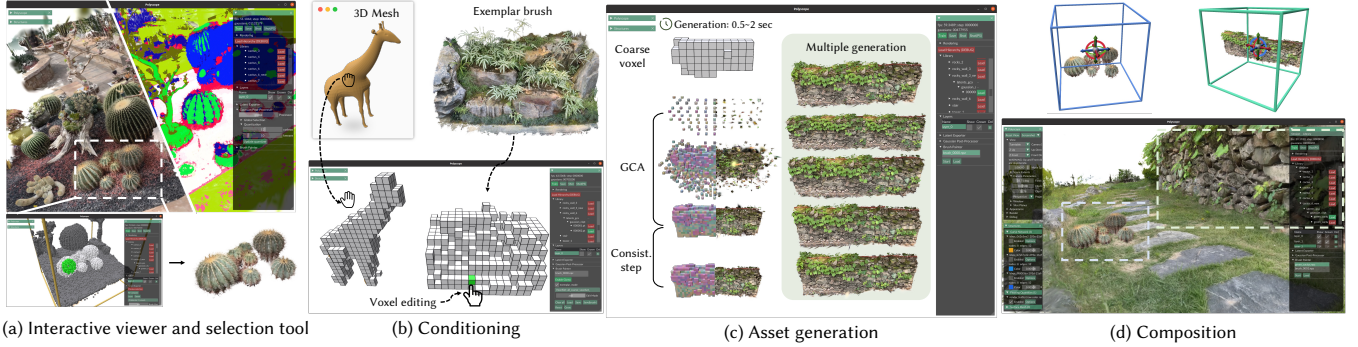


Fig. 3. Illustration of our user interface. (a) Our interactive viewer runs at real-time framerates (30-60fps) and comes with a selection tool using the quantized DINO features. Additional adjustments can be made at any stage with a manual selection tool. (b) Conditioning can be performed using “exemplar brushes,” voxelized 3D meshes, or direct voxel editing. (c) From this coarse conditioning signal, diverse assets can be generated using GCA and a subsequent patch consistency step. (d) Multiple generated assets can be composited into a single scene within our editor.

### 3.2 Technical Overview

We adapt 3D Gaussian Splatting [Kerbl et al. 2023] to reconstruct a scene from various casual user inputs as a high-quality appearance model similar to NeRF [Mildenhall et al. 2021] (Section 4.1). 3D Gaussians can be rendered at interactive rates with explicit entities, which naturally allows the manipulation and composition of complex scenes. However, individual 3D Gaussians are scattered within the scene and it is hard to manipulate them as they miss structure, such as connectivity. As described in Section 4.2, we augment 3D Gaussians with semantically-aware features distilled from foundation models, namely DINO [Caron et al. 2021; Oquab et al. 2023]. These features provide a means to aggregate semantically similar clusters, which can suggest intuitive segments of objects or regions of interest within the scene. More concretely, in Section 4.3, we describe our selection mechanism in which the user can interactively examine the space of suggested clusters with different levels of grouping, exploiting features from foundational models. Our proposed approach approximates the latent space in reduced dimensions such that the clustering remains fast and tractable to quickly cover multiple levels of clusters with reasonable coherency.

Then we seek to turn this selection into a controllable generative model trained from a single exemplar. Compared to conventional generative models that use extensive data, our primitives are extracted *tabula rasa*, requiring a radically different generative model. We thus propose to train a low-dimensional generative model, detached from the task of learning appearance, to impose appropriate inductive bias despite using a single exemplar. Our generative model focuses on low-resolution sparse voxel grids with coarse conditioning (Section 4.5). Individual grid cells contain multiple Gaussian splats, augmented with semantically-aware features used in the selection step. We employ *Generative Cellular Automata* (GCA) as a fast and data-efficient generative model that operates on regularly-structured sparse voxels, presented in Section 5.1. Our generative tool adapts GCA for controllable generation and single-exemplar training (Section 5.2).

Finally, we remap and refine the low-dimensional generation of GCA to the appearance space of the exemplar for high-quality

rendering (Section 5.3). Given the initial generation from the GCA composed of featured voxels, we introduce a *sparse* patch consistency operation on these voxels and subsequently fill them with the 3D Gaussians from the initial exemplar. While concurrent works use patch-based synthesis [Li et al. 2023] as a generative prior to produce hierarchically the radiance volume of natural scenes in a *dense* manner, we rely on patch-based synthesis as a final *consistency* step with minor changes to the voxels generated by GCA (see Figure 8).

## 4 PREPARATION

### 4.1 Background: 3D Gaussian Splatting

3D Gaussian Splatting [Kerbl et al. 2023] represents scenes as a set of  $N$  3D anisotropic Gaussians with positions  $\mu \in \mathbb{R}^3$  and covariance matrices  $\Sigma \in \mathbb{R}^{3 \times 3}$  parameterized by a scaling vector  $\mathbf{s} \in \mathbb{R}^3$  and a rotation quaternion  $\mathbf{r} \in \mathbb{R}^4$ . Their appearance is described by an opacity coefficient  $\eta \in \mathbb{R}$  and a view-dependent color  $\mathbf{c} : \mathbb{R}^3 \rightarrow \mathbb{R}^3$  originally parameterized by spherical harmonics with coefficients  $\boldsymbol{\gamma} \in \mathbb{R}^m$  (where  $m$  is typically 16 for spherical harmonics of degree 3). 3D Gaussians are rendered and optimized through a differentiable alpha-compositing rasterization algorithm as follows:

$$C = \sum_i \mathbf{c}^{(i)} \alpha^{(i)} \prod_{j=1}^{i-1} (1 - \alpha^{(j)}), \quad \text{where } \alpha^{(i)} = \eta^{(i)} G_{2D}^{(i)}(\mathbf{x}) \quad (1)$$

and  $G_{2D}^{(i)}(\mathbf{x})$  is the 2D linearized Gaussian density kernel of 3D Gaussian  $i$  after projecting it on the 2D viewplane. Please refer to [Kerbl et al. 2023] for more details on the rendering algorithm.

### 4.2 3D Gaussians Augmented with Semantically-aware Features

Given the unstructured mixture of independent Gaussians, we augment them with additional semantically-aware features  $\mathbf{f} \in \mathbb{R}^d$ . More precisely, we rely on DINO features [Caron et al. 2021; Oquab et al. 2023], which have shown robust performance across various tasks, including zero-shot segmentation. As these features are

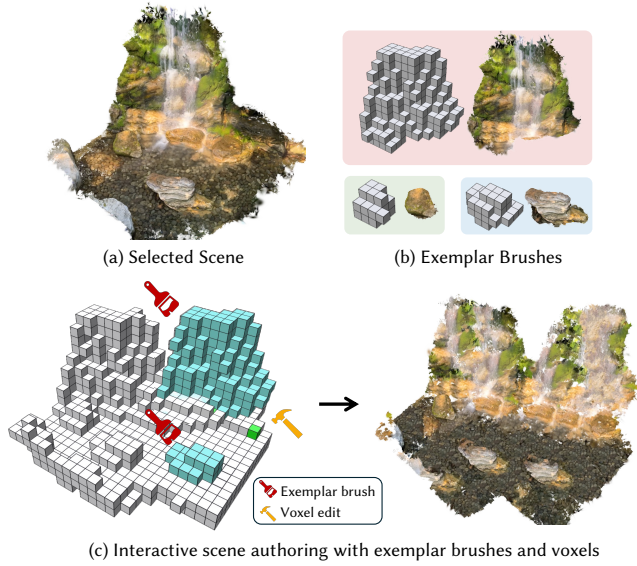


Fig. 4. From a selected scene, “exemplar brushes” representing regions of the scene, such as the waterfall or rocks, can be extracted within our editor. Authoring can then be performed coarsely by resampling these primitives and/or directly editing the voxels.

defined as 2D feature maps, we distill them in 3D by simply substituting  $\mathbf{f}^{(i)}$  to  $\mathbf{c}^{(i)}$  in Equation 1. Contrary to colors, we assume they are view-independent. Additional implementation details are provided in Appendix C.1.

The features provide coarse semantic information to guide our semi-automatic selection tool (Section 4.3) and our generative model (Section 4.5). However, DINO features have high dimensions by default, typically 756, which would induce a significant memory and computational cost with a large number of Gaussians and be a more complicated signal to model in the generative task. Consequently, we reduce their dimension by applying a joint PCA across all the feature maps extracted from the training images. For simplicity and efficiency, we choose  $d = 8$ . We use DINOv1 features [Caron et al. 2021] as we observed artifacts when extracting DINOv2 features [Oquab et al. 2023] as reported in previous works [Yang et al. 2023].

### 4.3 Suggestive Selection Mechanism

Real-world scenes captured by users often contain diverse backgrounds and surrounding objects without clear boundaries. This thus calls for an intuitive selection mechanism. We interactively provide a suggestive selection by aggregating regions with similar features. More precisely, we quantize the feature field using standard  $k$ -means clustering, where the user can manually adjust the number  $k$  of clusters. Due to its simplicity, this operation can be performed interactively, forming an intuitive workflow as shown in Figure 19 (Appendix D). Furthermore, selected regions can be refined by applying subsequent annotation steps or by selecting/pruning sets of 3D Gaussians with an interactive tool we show in Figure 3.a (bottom) and in the supplementary video.

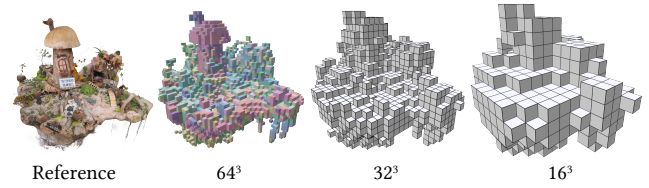


Fig. 5. Starting from an arbitrary set of anisotropic 3D Gaussians (left), we build a hierarchy of voxels, each bearing a unique feature. The finest level is progressively downsampled to produce coarser levels. Ultimately, only two levels will be used: a coarse conditioning resolution and a finer target resolution for generating sparse voxels. Features are only retained for the target resolution.

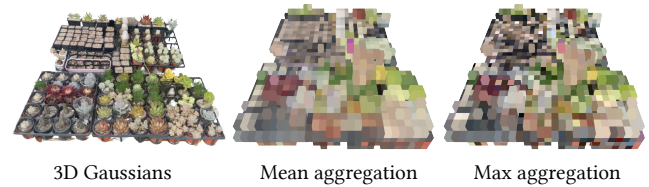


Fig. 6. Averaging features of Gaussians within a given voxel tends to “wash out” statistics (center). We thus prefer to pick the feature of a single representative Gaussian (right), which we choose to be the highest opacity one. In this figure, we show this at a coarse resolution and on RGB colors directly for visualization purposes.

### 4.4 User Conditioning

This 3D annotation mechanism is directly used to produce coarse “*exemplar brushes*” through which users can paint regions illustrated in Figure 4.b. This system nudges users to stay close to the distribution captured by our generative model throughout authoring.

Pruning the initial set of 3D Gaussians is not only beneficial to isolate the region of interest but it also provides the generative model with a precise and well-behaved distribution. We highlight this in Section 7.2 and Figure 14.

### 4.5 Preparing a Sparse Feature Grid

Given a region or an object selected by a user, we convert the corresponding set of 3D Gaussians and their features into a low-dimensional and regular spatial representation, facilitating the training of our 3D generative models conditioned on user inputs. We maintain the process fast and memory-efficient by employing sparse 3D voxels.

Each Gaussian is associated with a grid cell based on its center  $\mu$  position, and we instantiate a voxel only if there exists a Gaussian whose opacity  $\eta$  exceeds a given threshold  $\eta_{\text{thres}} = 0.1$ . We call these voxels “surface voxels”. We build a hierarchy of surface voxels  $\mathcal{V} = (V_i)$  to enable generation and conditioning at different resolutions. Each level is obtained by downsampling the previous one starting from the finest resolution:  $V_0 : 128^3 \rightarrow V_1 : 64^3 \rightarrow V_2 : 32^3 \rightarrow V_3 : 16^3$ , as illustrated in Figure 5. Only two resolutions (“coarse” and “target”) will be retained for the generative modeling task described

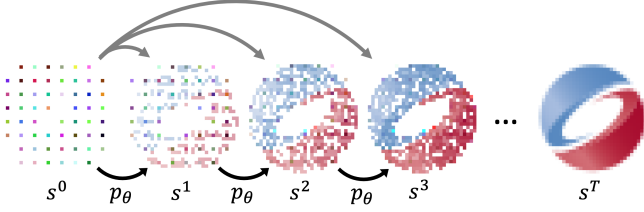


Fig. 7. At each time step  $t$ , GCA samples a new state  $s^{t+1}$  composed of sparse voxel occupancies equipped with features from  $p_\theta(s^{t+1}|s^t, s^0)$ . Recursively applying the transition kernel  $p_\theta$  to the initial state  $s^0$  yields the final generated state  $s^T$ . We adapt GCA to conditional generation by choosing  $s^0$  to be the upsampled coarse set of conditioning voxels and concatenating it to  $s^t$  each time  $p_\theta$  is applied (gray arrows on the top).

in Section 5.2. We discuss the trade-offs between these resolutions in Section 7.2.

Instead of learning a per-exemplar latent space with an auto-encoder [Wu et al. 2023], we rely directly on our field of 3D Gaussians and assign each voxel a feature. When assigning a voxel its feature, the corresponding feature should uniquely represent an arbitrarily large number of 3D Gaussians contained within the cell. Figure 6 shows that naïve averaging would destroy information. To mitigate this, we propose to select the Gaussian with the highest opacity, which contains more distinctive evidence. To maximize the amount of information from the scene and facilitate the low-dimensional conditional generative modeling task presented in Section 5, we choose this feature to be a mixture of appearance features and semantic features. In our case, this means spherical harmonics coefficients and the distilled DINO features presented in Section 4.2. In practice, we use four dimensions for each of them, resulting in an 8-dimensional feature per voxel. For consistency, each of them is *independently* PCA-ed and subsequently re-normalized.

## 5 LEARNING SPECIALIZED GENERATIVE PRIMITIVES

To learn a generative prior on sparse voxels, we adapt *Generative Cellular Automata* (GCA) [Zhang et al. 2021, 2022]. At a high level, our generative model is only trained to predict occupied surface voxels and their corresponding features as described in the previous section.

### 5.1 Background: *Generative Cellular Automata*

GCA represents shapes as a set of sparse voxels, also denoted as cells, equipped with features,  $s = \{(c, o_c, z_c) | c \in \mathbb{Z}^3, o_c \in \{0, 1\}, z_c \in \mathbb{R}^K\}$ , where  $o_c$  denotes the binary occupancy of a cell,  $c$  its coordinates and  $z_c$  the feature attached to the cell  $c$ . Given an initial state  $s^0$ , GCA generates a completed state  $s^T$  by recursively sampling intermediate states  $s^{1:T} = \{s^1 \rightarrow \dots \rightarrow s^T\}$ :

$$s^{t+1} \sim p_\theta(\cdot | s^t), \quad (2)$$

where  $T$  is a predefined number of transition steps and  $p_\theta$  is a local transition kernel with parameters  $\theta$ . The process is illustrated in Figure 7. The transition kernel is parameterized as a U-Net [Ronneberger et al. 2015] and uses sparse convolutions [Graham et al. 2018], which are crucial to process data efficiently in 3D. At a given

time step  $t$ , only transitions in the direct neighborhood of occupied cells are considered. The neighborhood of a state is defined as  $\mathcal{N}(s^t) = \{c' \in \mathbb{Z}^3 | d(c, c') \leq r, o_c = 1, c \in \mathbb{Z}^3\}$  where  $d$  is the L1 distance. To keep inference tractable, transition kernels are factorized for each cell in  $\mathcal{N}(s^t)$  independently (Eq. 3) and the distribution of a single cell  $p_\theta(o_c, z_c)$  is further decoupled into occupancy  $o_c$  followed by  $z_c$  (Eq. 4):

$$p(s^{t+1}|s^t) = \prod_{c \in \mathcal{N}(s^t)} p_\theta(o_c, z_c | s^t) \quad (3)$$

$$= \prod_{c \in \mathcal{N}(s^t)} p_\theta(o_c | s^t) p_\theta(z_c | s^t, o_c). \quad (4)$$

Binary occupancy transition kernels are parameterized as Bernoulli distributions while feature kernels are parameterized as Gaussian distributions

$$p_\theta(o_c | s^t) = \text{Ber}(\lambda_{\theta, c}), \quad (5)$$

$$p_\theta(z_c | s^t, o_c) = \begin{cases} \delta_0 & \text{if } o_c = 0 \\ N(\mu_{\theta, c}, \sigma^t \mathbf{I}) & \text{if } o_c = 1. \end{cases} \quad (6)$$

where  $\lambda_{\theta, c} \in [0, 1]$  and  $\mu_{\theta, c}$  are directly predicted by the U-Net and  $\delta_0$  is a Dirac delta distribution indicating that  $z_c = 0$  when  $o_c = 0$ . For occupied voxels ( $o_c = 1$ ),  $z_c$  follows a normal distribution whose standard deviation  $\sigma^t$  is progressively annealed during sampling.

GCA is trained through a process called *Infusion* [Bordes et al. 2017], which we describe and discuss further in Appendix A. Intuitively, starting from a state  $s^0$ , *Infusion* supervises the learned transition kernel  $p_\theta(s^{t+1}|s^t)$  to stay close to an “infused kernel” biased towards a target shape  $x$ .

### 5.2 Extending GCAs to Single-exemplar Training and Controllable Generation

A challenge in our setting arises from the fact that we wish to learn a distribution from a single exemplar. As we ablate in Section 7.1, using the original U-Net architecture of GCA [Zhang et al. 2021, 2022] causes direct overfitting on the input exemplar. To tackle this issue, we build on the observations from previous works that train generative models from a single image or shape [Nikankin et al. 2022; Wang et al. 2022a] and propose to severely hinder the receptive field of the U-Net by only performing one downsampling operation and using very shallow ResNet blocks. Additionally, we show that training on smaller, yet not too small, crops of the original shape [Wu et al. 2023] helps the network learn local structure in a moderately generalizable manner. Full implementation details are provided in Appendix C.2.

Another key objective of our method is control. To make shape generation conditional, we leverage the explicit nature of sparse voxel generation in GCA. More concretely, from the voxel hierarchy  $\mathcal{V}$  introduced in Section 4.5, we select a target resolution  $r_t$  (e.g.,  $64^3$ ) and a coarse conditioning resolution  $r_c$  (e.g.  $16^3$ ). Given a coarse geometric input shape at resolution  $r_c$ , we upsample the corresponding set of voxels to target resolution  $r_t$ . We use the corresponding cells as the initial state  $s^0$  and to provide an actual conditioning



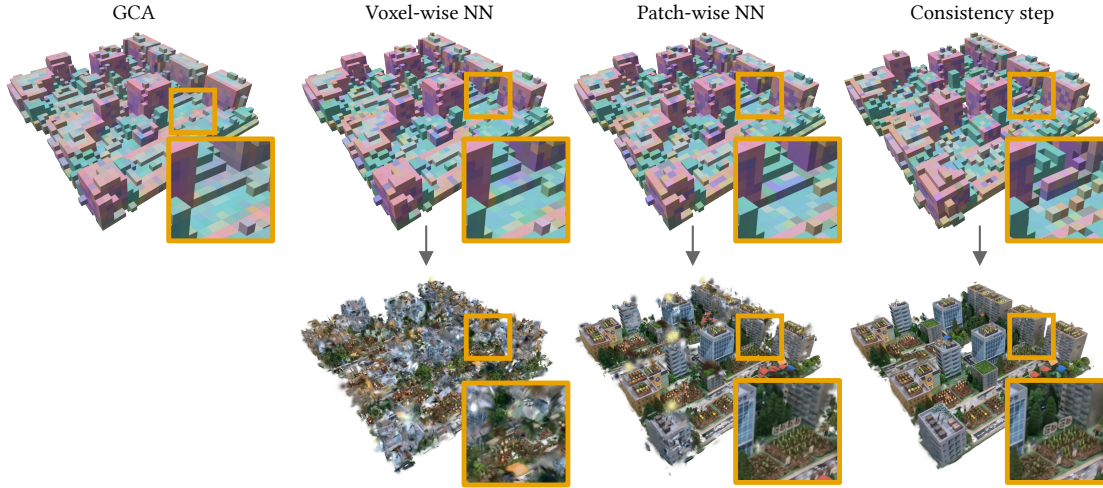


Fig. 8. GCA is only trained to predict occupancy and a feature for each voxel. *Voxel-wise NN*. Naively remapping each predicted voxel to its nearest feature in the exemplar and filling in the corresponding 3D Gaussians fails to produce consistent results due to local consistency and the approximate predictions of GCA. *Patch-wise NN*. Using the patch-wise distance defined in Equation 7 improves visual coherence but still fails to account for modeling errors. *Consistency Step*. We thus propose an additional sparse patch consistency operation to refine missing local statistics.

signal to GCA, we also concatenate them as an additional input to the network at every step  $t$ . Note that features are initialized at random following a standard normal distribution. In other words, we only condition on coarse geometry. Our GCAs are then trained to produce the reference shape and features at resolution  $r_t$  by sampling  $s^{1:T}$ . Figures 1 and 3.c illustrate the practical conditioning and sampling process. During training, the conditioning shape is the reference shape (i.e., teacher-forcing) while at inference, this can be any coarse voxelized shape derived from a mesh, a region from another scene, a subset of voxels from the current scene, etc. As we show in Section 7.2, the relative choice of  $r_t$  and  $r_c$  is crucial to produce controllable and diverse outputs. If not mentioned, we use  $r_t = 64^3$  and  $r_c = 16^3$ .

### 5.3 Sparse Patch Consistency Step

Since the above-mentioned generative model only predicts voxel occupancies and features, we must remap this low-dimensional output to the pre-existing (selected) set of Gaussians of the exemplar scene. As a first naive approach, we can easily map each generated voxel to its nearest neighbor in the exemplar with respect to the predicted feature, we denote this as “Voxel-wise NN”. As shown in Figure 8, this approach fails to produce consistent results as each voxel is considered independently from its neighbors. Using a patch-wise distance to find nearest neighbors, denoted as “Patch-wise NN”, brings partial consistency but the result remains unsatisfactory as it ignores shared local coherence between voxels and does not account for voxels that GCA might have failed to generate.

To tackle this problem, we draw inspiration from the image-processing literature with an additional patch consistency operation. Patch-based synthesis was originally introduced on images for which the domain is dense and simple per-pixel metrics can be directly applied. However, in 3D, we need to account for the notion

of occupancy. To side-step the problem, Sin3DGen [Li et al. 2023] converts the radiance volume into a *dense* bounded signed distance field by *flood filling* unoccupied cells. Approximate matching with PatchMatch [Barnes et al. 2009] (i.e., using a *Nearest Neighbor Field*) is then applied at multiple resolutions based on a weighted L2 distance between geometric and appearance features. On the other hand, we wish to retain sparsity throughout the whole process. To do so, we introduce a distance that operates directly on sparse voxels. We further discuss the differences between our approach and Sin3DGen in Appendix B.

Let  $P_i = (\mathbf{O}_i, \mathbf{F}_i)$  be an arbitrary patch where  $\mathbf{O}_i \in \{0, 1\}^p$  is the occupancy within the patch,  $\mathbf{F}_i \in \{0, 1\}^{p \times d}$  the features within the patch and  $p = l^3$  the patch size. At each iteration, we consider only patches centered at surface voxels. Given a patch  $P_e$  (resp.  $P_g$ ) in the exemplar (resp. in the generated shape), our distance is given by:

$$d(P_e, P_g) = (1 - w) d_{\text{occ}}(P_e, P_g) + w d_{\text{feat}}(P_e, P_g), \quad (7)$$

where

$$d_{\text{occ}}(P_e, P_g) = 1 - \frac{\mathbf{O}_e \cdot \mathbf{O}_g}{p}, \quad (8)$$

$$d_{\text{feat}}(P_e, P_g) = 1 - \frac{\mathbf{F}_e \cdot \mathbf{F}_g}{\mathbf{O}_e \cdot \mathbf{O}_g}. \quad (9)$$

The dot product  $\mathbf{F}_e \cdot \mathbf{F}_g$  in Equation 9 can be directly interpreted as a “masked” *cosine similarity* between the corresponding features. This holds because these features are normalized as presented in Section 4.5 (i.e., with values in  $[-1, 1]$ ) and because we give unoccupied voxels within a patch a zero feature. In practice, we independently normalize each component of our mixture of features introduced in Section 4.5, i.e., appearance and semantic features. Consequently, we implement  $d_{\text{feat}}$  as two independent distances that we simply average. The re-normalization term in Equation 9 guarantees that we don’t prioritize patches with fewer intersecting voxels but consistent



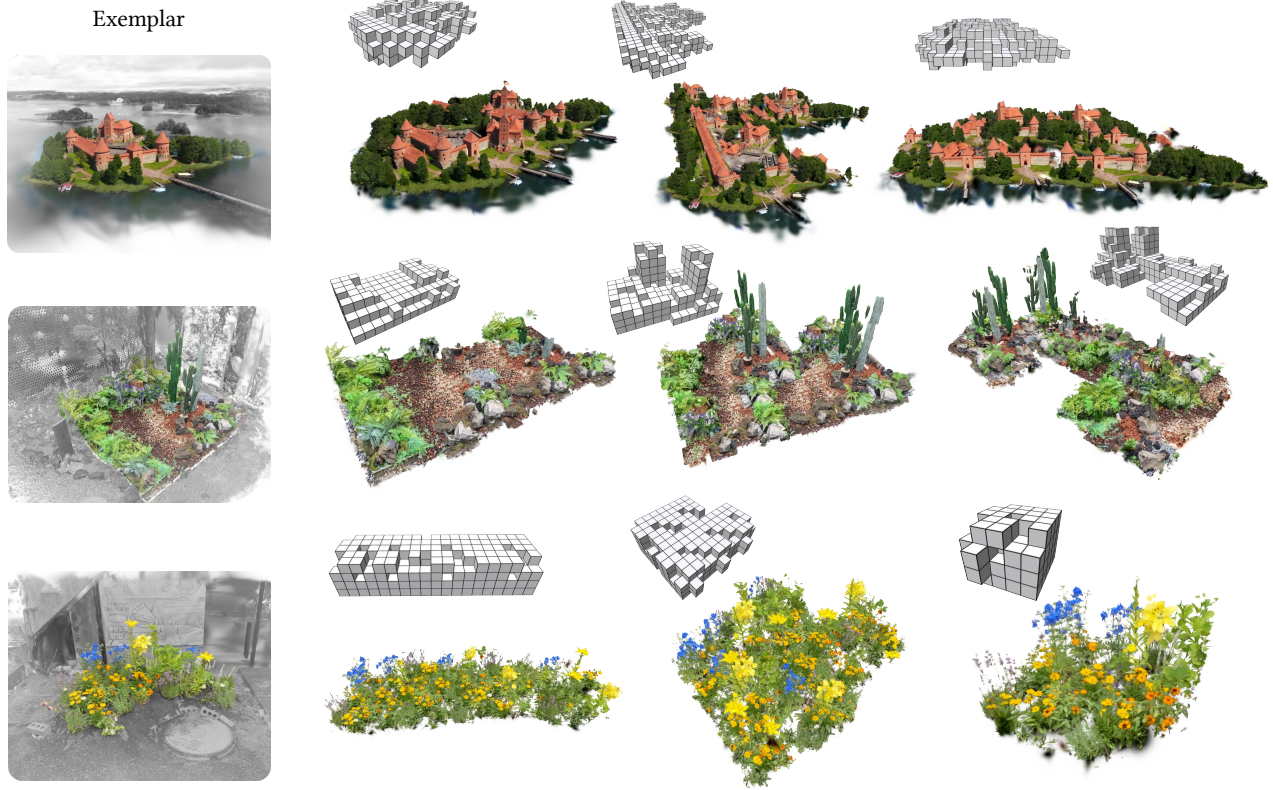


Fig. 9. Starting from the exemplar on the left, we demonstrate various results generated by each corresponding primitive given different conditioning shapes. All examples are derived from real scenes. The first row is based on a drone video found on Youtube.

matching features. As we proceed sparsely, we can even perform an exhaustive matching operation. After matching, we blend features by averaging them weighted by occupancy to consider only the contribution of overlapping features. Moreover, at each step, we update occupancy based on a *voting strategy* where a voxel is considered occupied if the proportion of occupied voxels in all overlapping patches reaches a threshold  $\beta$  (chosen to be 0.5 in our experiments). In addition to matching features locally with the exemplar, this also enables us to grow and ungrow voxels. As this should only yield small refinements, we limit additional voxels from being added farther than a distance  $\lambda_{\text{patch}}$  from the initial shape generated by GCA. In practice, we use a patch size of  $l = 5$ , 7 iterations and  $\lambda_{\text{patch}} = 2$ .

## 6 SCENE AUTHORING RESULTS

### 6.1 User Interface

We embed the previously described technical components into an intuitive user interface depicted in Figure 3. This interface builds on the real-time capabilities of 3D Gaussian Splatting and comes with an interactive 3D viewer that allows one to navigate scenes and select objects with the guidance of the mechanism described in Section 4.3. Additional refinement can be performed using a manual selection tool. Note that it is also possible to select regions directly from this tool. Control is achieved through coarse geometry from any input that can be turned into a coarse voxel grid. In practice,

we provide 3 input types shown in Figure 3.b: 3D meshes, “exemplar brushes” and direct voxel editing. All of them can be used interchangeably and in a fully composable manner.

The generation process is illustrated in Figure 3.c. Given the coarse conditioning voxels, GCA generates a finer featurized voxel grid that is subsequently remapped to 3D Gaussians through our patch consistency step. For visual feedback during generation, we visualize the growing process using “Voxel-wise NN” matching as introduced in Section 5.3 and shown in Figure 8. The complete sampling including the consistency step process takes 0.5 to 2 seconds, thus allowing multiple samples to be drawn until satisfaction. Each generated shape from a given specialized primitive is denoted as a “layer”, similar to existing 2D tools [Adobe Inc. 2024b]. At any time, users can choose to resample primitives. Layers can be composed, duplicated, displaced, rotated, etc. We also provide an additional tone-mapping tool to adjust the color of 3D Gaussians and support for environment maps as can be seen in Figure 1.

### 6.2 Creations

To showcase our method, we manually created a variety of primitives entirely within our user interface. To illustrate the practical feasibility of our method, these primitives were extracted and trained from videos we captured directly from our smartphones, except for the two aisles in Figure 18, which were taken from the LeRF

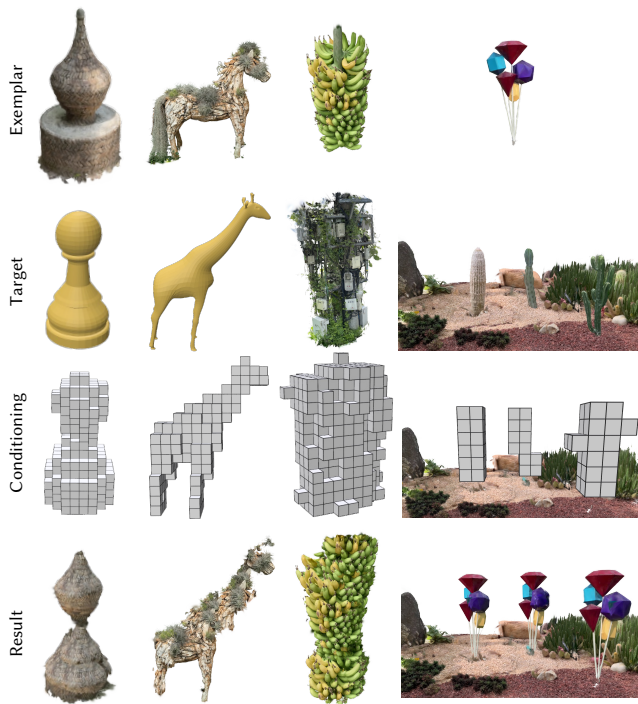


Fig. 10. Our primitives can be used to transfer appearances to a mesh (columns 1-2) or another primitive (column 3). More precisely, given an input exemplar (row 1), and a target geometry (row 2), the target geometry is converted to conditioning voxels (row 3), and the exemplar primitive is used to generate a new result (row 4). In the right-most example, we show that with additional manual intervention, this idea can be pushed to perform more complex edits between scenes. Here, the sculptures were directly generated using the conditioning shown on the third row and the original cactuses were removed manually with our selection tool.

dataset [Kerr et al. 2023] and two Youtube videos <sup>1</sup>. In other words, all the scenes we used are *real* and not synthetic. Figure 9 shows generated results given various conditional inputs. Figure 18 in Appendix D shows that the same conditioning input leads to diverse generated results. In Figure 10, we show that our method can also be used to transfer the appearance of a given exemplar to other geometries or to compose multiple scenes. Finally, in the supplemental video, we provide an example of a full authoring session during which multiple primitives are used and composed interactively.

## 7 TECHNICAL ANALYSIS

We implement our framework in Python using a custom version of Polyscope [Sharp et al. 2019] as our front-end viewer. Providing a high-level and accessible codebase to benefit scientific and creative communities was a key design choice. Our 3D Gaussian Splatting renderer is built on top of *gsplat* v0.1.11 [Ye et al. 2024] and a few

<sup>1</sup>The island in Figure 9 was captured by @travelpixified: <https://tinyurl.com/ckjrufz8>. The village in Figures 1 and 18 was captured by @4kdronefootage: <https://tinyurl.com/h5b99mbp>

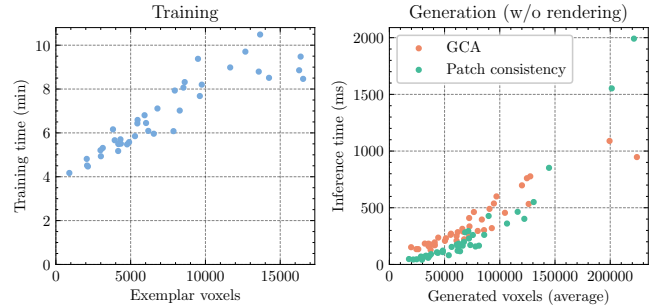


Fig. 11. Online timings for training (left) and generation (right). We report training times for 40 manually designed primitives across various objects and regions (left). Even for a large number of voxels in the input exemplar, training time is almost always below 10 minutes. Conditioned on each manual input, we generate 10 samples and report the average generation time for GCA (red, right) and the subsequent patch consistency operation (green, right). Generation in sum takes less than 2 seconds in most cases.

Table 1. Using more lightweight U-Nets also implies smaller model sizes and faster training and generation times (without the consistency step). All values were obtained on the primitive shown in Figure 12. Inference timings were averaged over 10 generated samples.

	Model size	Training	Generation
U-Net Light (depth=1)	0.95 MB	4.54 min	198.89 ms
U-Net Light (depth=2)	4.21 MB	6.25 min	199.98 ms
U-Net Light (depth=3)	17.12 MB	7.61 min	215.78 ms
cGCA [Zhang et al. 2022]	468.19 MB	23.40 min	328.74 ms

additional routines from *nerfstudio* [Tancik et al. 2023]. Our implementation of GCA is based on Zhang et al. [2021, 2022] and uses MinkowskiEngine [Choy et al. 2019] for sparse tensor computations. Additional implementation details are provided in Appendix C.

The experiments throughout this section were performed on a desktop with an AMD Ryzen 7 7700 CPU (8 cores), 32 GiB of RAM, and an NVIDIA GeForce RTX 4090 (24 GiB of VRAM). We use Linux kernel 6.5.0, Python 3.11.8, CUDA 11.8, and NVIDIA driver 550 on the software side.

### 7.1 Model Architecture & Random Augmentations

A crucial design choice to train GCA on a single exemplar comes from the architecture of the network. As shown in Figure 12, naively using the deep U-Net architecture proposed by Zhang et al. [2022], denoted as cGCA, results in plain overfitting on the input shape and appearance. This can be explained by both the large receptive field and the model capacity of the original backbone. To mitigate this effect, we propose a lighter model composed of a single ResNet block per resolution with 16 base channels and channels multiplied by 2 for each resolution. In Figure 12 and Table 1, we use “U-Net Light (depth= $n$ )” to designate this architecture with  $n - 1$  contractions. “U-Net Light (depth=2)” strikes a good balance between diversity and structure. We thus choose it as our base architecture. Additionally, as shown in Table 1, using a dramatically smaller network significantly boosts training and inference speed. This is key to a

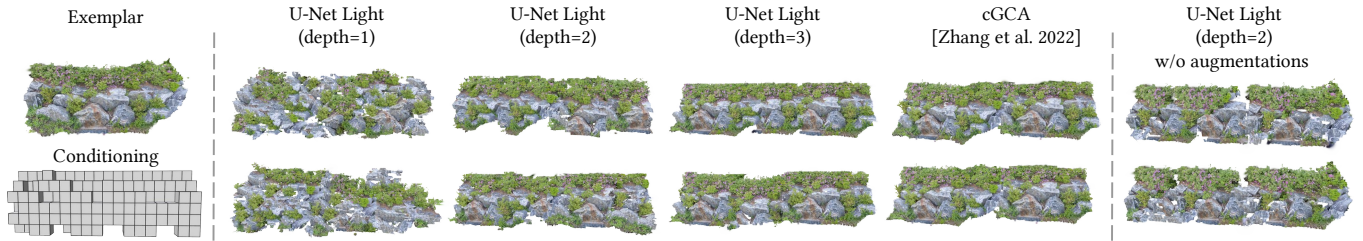


Fig. 12. Given the input exemplar on the left, we train GCA with various architectures with different receptive fields. We then generate multiple samples with a larger input conditioning signal. Even with a small number of parameters, a too-large receptive field (i.e., U-Net Light (depth=3)) yields samples with low diversity and large redundant blocks. Conversely, a too-small receptive field (i.e., U-Net Light (depth=1)) causes the network to produce too unstructured samples, often partially satisfying the conditioning signal. Even with a smaller receptive field, models trained without random augmentations produce samples with low diversity and discontinuities matching the limits of the input exemplar (right-most column).

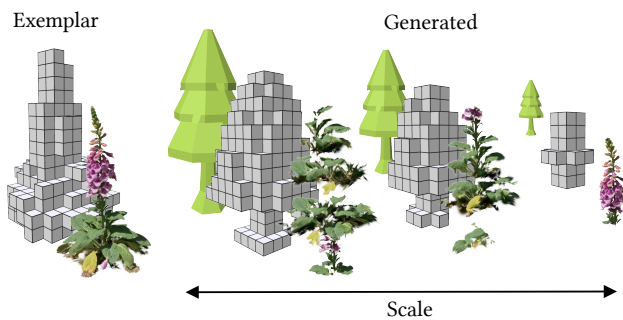


Fig. 13. From a given input exemplar on the left, we generate a shape given the same input mesh at different scales. Note that the mesh is always voxelized to condition generation. Far from the structural distribution of the input exemplar, the primitive fails to produce consistent outputs.

tractable workflow where users can interact with primitives they prepared without long training times. We report the training and generation performance of our method in Figure 11.

Incorporating random crops of the original set of voxels enhances the diversity of generated results despite training primitives with a limited set of inputs. The results in the right-most column of Figure 12 exhibit discontinuities with limited diversity without such random augmentations.

## 7.2 Voxels for Generative Primitives

In Section 4.5, we introduced a voxel hierarchy with multiple resolutions. In Figure 21 (Appendix D), we highlight the trade-offs between each resolution for conditioning and generation. The relative scales between the conditioning and the target are crucial to balance fidelity and diversity. Building on these observations, we choose  $r_t = 64^3$  and  $r_c = 16^3$  as a compromise. This implies a generation-to-conditioning ratio of 4.

Being trained on a single exemplar without external priors, our generative model cannot extrapolate to inputs that are structurally too far from its initial distribution. We illustrate this phenomenon in Figure 13. For the same reason, it is also essential to carefully select the target distribution of the primitive. As shown in Figure 14, properly isolating flowers from their pot allows us to use the brush

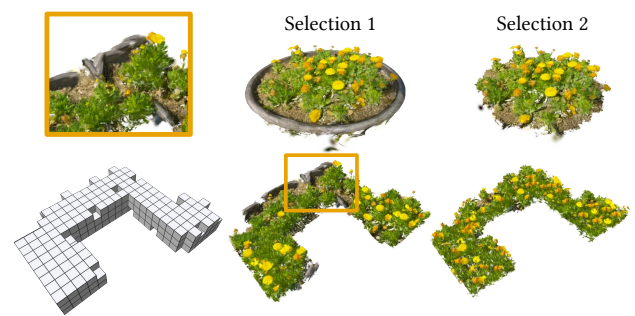


Fig. 14. With two different selections of the same scene, generalization can be severely hindered by structural artifacts that lie beyond the invariances that can be captured by GCA as it operates on axis-aligned voxel grids.

without artifacts in a more general context. As each primitive is only conditioned through coarse voxels, ambiguities appear for complicated scenes where the same coarse geometry may be partially repeated throughout the scene. Since our GCA cannot observe the full generation, this results in “out of place” generated results as illustrated in Figure 15.

Another issue arises from the limits of a given selection. Both GCA and our patch consistency step attribute a specific geometric feature to irregular boundaries that they try to reproduce during generation. We illustrate this phenomenon in Figure 20 (Appendix D).

## 7.3 Sparse Patch Consistency Step

In Figure 22 (Appendix D), we show the impact of each parameter of our sparse patch consistency operation. In the first row, we illustrate the impact of patch size  $p = l^3$ . A small patch size length (i.e.,  $l = 3$ ) matches local statistics and ignores structure. A large patch size leads to more intensive computations (especially for a large number of voxels) without significant improvements. Our patch consistency is evaluated by combining the occupancy  $d_{occ}$  and the feature distance  $d_{feat}$  as presented in Equation 7. Biasing the total distance towards the occupancy term  $d_{occ}$  causes the algorithm to match dominant geometric statistics, which results in local flattening and repetitions. On the other hand, biasing it towards the feature term  $d_{feat}$  leads to

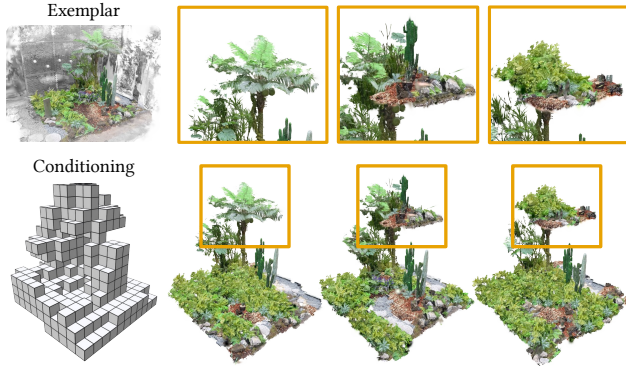


Fig. 15. Due to its limited receptive field and capacity, our model can confuse some regions with others during generation. This is particularly noticeable when the distribution of the exemplar is too diverse (i.e., scene-level) and different regions with different semantics share the same coarse geometry.

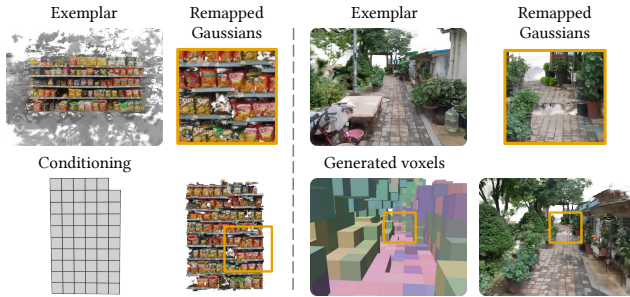


Fig. 16. Our method operates on fixed-size voxels that can only be retrieved from the set of voxels in the exemplar. For axis-aligned structured primitives (left) and large-scale primitives (right), this comes with noticeable artifacts, namely misalignment (left) and cracks (right).

severe artifacts. The expansion distance  $\lambda_{\text{patch}}$  defines the possible deviation range from the original generated voxels. The last row shows that a small  $\lambda_{\text{patch}}$  may severely confine the patch consistency step to the possibly erroneous output of GCA and lead to incomplete objects. On the other hand, a large value leads to spurious and uncontrolled expanded regions. Note that by default, we always use a patch size of length  $l = 5$ , 7 iterations,  $w = 0.5$  for the weight between the occupancy distance  $d_{\text{occ}}$  and the feature distance  $d_{\text{feat}}$ , and a maximum expansion distance  $\lambda_{\text{patch}} = 2.0$ .

Treating appearance and geometry as fixed-size voxels that are only resampled from the exemplar naturally introduces discontinuities, as shown in Figure 16. This can occur because the selection bounding box is not perfectly aligned with the structure of interest, the practical size of a voxel does not match the local structure of the exemplar, or because there is simply no way to bind two such regions of the scene. This phenomenon becomes particularly noticeable when training primitives on very large distributions (e.g., entire scene), as shown on the right of Figure 16.

## 8 CONCLUSION & DISCUSSION

We propose “Specialized Generative Primitives”, a lightweight and compositional generative framework to author high-quality 3D scenes from casual user inputs through coarse conditioning. Key to our method is the ability to perform every step of our pipeline, from preparation to composition, within an interactive viewer. Each specialized primitive is obtained from a single *real-world* exemplar captured within a video. We use 3D Gaussian Splatting as a fast and detailed appearance model. We adapt Generative Cellular Automata as an efficient and controllable generative model. Our choice of a voxelized representation suggests an approximate geometric layout and allows explicit user edits. We achieve single-exemplar training of GCA by using a low-dimensional representation detached from the complexity of 3D Gaussians, injecting semantically-aware features, and employing a small network trained with random augmentations. Training our primitives takes less than 10 minutes. Finally, we propose a sparse patch consistency step to efficiently transform the coarse-generated voxels into 3D Gaussians with a high-quality appearance. Complete generation takes 0.5 to 2 seconds for each primitive, enabling truly interactive authoring sessions. Through various examples, we show that our primitives can be used to model and author various distributions and enable diverse applications: scene composition, appearance transfer, mixing primitives and scenes and more.

*Limitations & future work.* Being trained from a single exemplar without additional external priors, our generative model naturally exhibits limited generalization capabilities. However, by relying directly on the input exemplar 3D representation, our appearance model directly reflects what is captured and selected by the user, thus providing a different aspect of controllability. A promising avenue could be to explore bridges with 3D generative models that employ large-scale priors. Conversely, distilling general priors into specialized representations like ours could offer compact, “resamplable”, and controllable alternatives to the currently frozen outputs of large models. Even if inference has been dramatically reduced, large-scale models remain multiple orders of magnitude bigger than ours and come with intensive computational requirements, precluding their use on edge devices.

Our appearance model uses the original form of 3D Gaussian Splatting [Kerbl et al. 2023] and may benefit from recent variations to overcome its inherent limitations. For example, splats reconstructed from casual user inputs may vary significantly in quality, especially when captured by non-experts. For these, solutions have recently been explored [Bulò et al. 2024; Kheradmand et al. 2024]. We may also integrate formulation to allow relighting of 3D Gaussians [Gao et al. 2023b]. While our generative backbone has low memory usage (Section 7.2), 3D Gaussians can exceed 1 GB for some primitives. By the same argument, we could leverage recent advances to compress 3D Gaussians [Lee et al. 2024; Papantonakis et al. 2024].

Since we seek a real-time and interactive solution, many components sacrifice precision and fine-grained control for efficiency. For example, our intuitive selection mechanism may explore more precise segmentation techniques, e.g., hierarchical grouping [Kim et al. 2024]. Furthermore, we could expand our axis-aligned random augmentations to allow other forms of invariances, such as rotation

or scaling, and incorporate more general patch consistency information at the expense of additional parameters [Barnes et al. 2010]. In Section 7.2, we showed that the choice of resolution is crucial for both generative modeling and defining the granularity at which a primitive can be controlled. Exploring automatic ways of defining such a resolution and scale could be an exciting direction for future works. A more complex solution would jointly train multiple nested models and use the one with a target level of granularity at which a user wishes to author content as suggested by recent multi-scale approaches [Rao et al. 2022; Ren et al. 2023].

## REFERENCES

- Adobe Inc. 2024a. *Adobe Illustrator*. <https://adobe.com/products/illustrator>
- Adobe Inc. 2024b. *Adobe Photoshop*. <https://www.adobe.com/products/photoshop.html>
- Adobe Inc. 2024c. *Substance 3D Modeler*. <https://www.adobe.com/products/substance3d/apps/modeler.html>
- Connelly Barnes, Eli Shechtman, Adam Finkelstein, and Dan B Goldman. 2009. Patch-Match: A randomized correspondence algorithm for structural image editing. *ACM Trans. Graph.* 28, 3 (2009), 24.
- Connelly Barnes, Eli Shechtman, Dan B Goldman, and Adam Finkelstein. 2010. The generalized patchmatch correspondence algorithm. In *Computer Vision—ECCV 2010: 11th European Conference on Computer Vision, Heraklion, Crete, Greece, September 5–11, 2010, Proceedings, Part III 11*. Springer, 29–43.
- Connelly Barnes and Fang-Lue Zhang. 2017. A survey of the state-of-the-art in patch-based synthesis. *Computational Visual Media* 3 (2017), 3–20.
- Jonathan T Barron, Ben Mildenhall, Dor Verbin, Pratul P Srinivasan, and Peter Hedman. 2023. Zip-nerf: Anti-aliased grid-based neural radiance fields. In *Proceedings of the IEEE/CVF International Conference on Computer Vision*. 19697–19705.
- Yash Bhalgat, Iro Laina, João F Henriques, Andrew Zisserman, and Andrea Vedaldi. 2024. N2F2: Hierarchical Scene Understanding with Nested Neural Feature Fields. *arXiv preprint arXiv:2403.10997* (2024).
- Florian Bordes, Sina Honari, and Pascal Vincent. 2017. Learning to Generate Samples from Noise through Infusion Training. In *5th International Conference on Learning Representations, ICLR 2017, Toulon, France, April 24–26, 2017, Conference Track Proceedings*. OpenReview.net. <https://openreview.net/forum?id=BJAFbaolg>
- Samuel Rota Bulò, Lorenzo Porzi, and Peter Kotschieder. 2024. Revising Densification in Gaussian Splatting. *arXiv preprint arXiv:2404.06109* (2024).
- Mathilde Caron, Hugo Touvron, Ishan Misra, Hervé Jégou, Julien Mairal, Piotr Bojanowski, and Armand Joulin. 2021. Emerging properties in self-supervised vision transformers. In *Proceedings of the IEEE/CVF international conference on computer vision*. 9650–9660.
- Qimin Chen, Zhiqin Chen, Hang Zhou, and Hao Zhang. 2023b. ShaDDR: Interactive Example-Based Geometry and Texture Generation via 3D Shape Detailization and Differentiable Rendering. In *SIGGRAPH Asia 2023 Conference Papers*. 1–11.
- Yiwen Chen, Zilong Chen, Chi Zhang, Feng Wang, Xiaofeng Yang, Yikai Wang, Zhonggang Cai, Lei Yang, Huaping Liu, and Guosheng Lin. 2023a. Gaussianeditor: Swift and controllable 3d editing with gaussian splatting. *arXiv preprint arXiv:2311.14521* (2023).
- Yang Chen, Yingwei Pan, Yehao Li, Ting Yao, and Tao Mei. 2023d. Control3d: Towards controllable text-to-3d generation. In *Proceedings of the 31st ACM International Conference on Multimedia*. 1148–1156.
- Zhiqin Chen, Thomas Funkhouser, Peter Hedman, and Andrea Tagliasacchi. 2023c. Mobilerf: Exploiting the polygon rasterization pipeline for efficient neural field rendering on mobile architectures. In *Proceedings of the IEEE/CVF Conference on Computer Vision and Pattern Recognition*. 16569–16578.
- Zhiqin Chen, Vladimir G Kim, Matthew Fisher, Noam Aigerman, Hao Zhang, and Siddhartha Chaudhuri. 2021. Decor-gan: 3d shape detailization by conditional refinement. In *Proceedings of the IEEE/CVF conference on computer vision and pattern recognition*. 15740–15749.
- Xinhua Cheng, Tianyu Yang, Jianan Wang, Yu Li, Lei Zhang, Jian Zhang, and Li Yuan. 2023. Progressive3d: Progressively local editing for text-to-3d content creation with complex semantic prompts. *arXiv preprint arXiv:2310.11784* (2023).
- Christopher Choy, JunYoung Gwak, and Silvio Savarese. 2019. 4D Spatio-Temporal ConvNets: Minkowski Convolutional Neural Networks. In *Proceedings of the IEEE Conference on Computer Vision and Pattern Recognition*. 3075–3084.
- Matt Deitke, Dustin Schwenk, Jordi Salvador, Luca Weihs, Oscar Michel, Eli VanderBilt, Ludwig Schmidt, Kiara Ehsani, Aniruddha Kembhavi, and Ali Farhadi. 2023. Objaverse: A universe of annotated 3d objects. In *Proceedings of the IEEE/CVF Conference on Computer Vision and Pattern Recognition*. 13142–13153.
- Daniel DeTone, Tomasz Malisiewicz, and Andrew Rabinovich. 2018. Superpoint: Self-supervised interest point detection and description. In *Proceedings of the IEEE conference on computer vision and pattern recognition workshops*. 224–236.
- Prafulla Dhariwal and Alexander Nichol. 2021. Diffusion models beat gans on image synthesis. *Advances in neural information processing systems* 34 (2021), 8780–8794.
- Olga Diamanti, Connelly Barnes, Sylvain Paris, Eli Shechtman, and Olga Sorkine-Hornung. 2015. Synthesis of complex image appearance from limited exemplars. *ACM Transactions on Graphics (TOG)* 34, 2 (2015), 1–14.
- Jan-Niklas Dihlmann, Andreas Engelhardt, and Hendrik Lensch. 2024. SIGNeRF: Scene Integrated Generation for Neural Radiance Fields. *arXiv preprint arXiv:2401.01647* (2024).
- Wenqi Dong, Bangbang Yang, Lin Ma, Xiao Liu, Liyuan Cui, Hujun Bao, Yuewen Ma, and Zhaopeng Cui. 2024. Coin3D: Controllable and Interactive 3D Assets Generation with Proxy-Guided Conditioning. *arXiv preprint arXiv:2405.08054* (2024).
- Daniel Duckworth, Peter Hedman, Christian Reiser, Peter Zhizhin, Jean-François Thibert, Mario Lučić, Richard Szeliski, and Jonathan T Barron. 2023. SMERF: Streamable Memory Efficient Radiance Fields for Real-Time Large-Scene Exploration. *arXiv preprint arXiv:2312.07541* (2023).
- Marek Dvorožňák, Daniel Šykora, Cassidy Curtis, Brian Curless, Olga Sorkine-Hornung, and David Salesin. 2020. Monster mash: a single-view approach to casual 3D modeling and animation. *ACM Transactions on Graphics (TOG)* 39, 6 (2020), 1–12.
- Mathias Eitz, James Hays, and Marc Alexa. 2012. How Do Humans Sketch Objects? *ACM Trans. Graph. (Proc. SIGGRAPH)* 31, 4 (2012), 44:1–44:10.
- Jennifer Fernquist, Tovi Grossman, and George Fitzmaurice. 2011. Sketch-sketch revolution: an engaging tutorial system for guided sketching and application learning. In *Proceedings of the 24th annual ACM symposium on User interface software and technology*. 373–382.
- Sara Fridovich-Keil, Alex Yu, Matthew Tancik, Qinhong Chen, Benjamin Recht, and Angjoo Kanazawa. 2022. Plenoxels: Radiance fields without neural networks. In *Proceedings of the IEEE/CVF Conference on Computer Vision and Pattern Recognition*. 5501–5510.
- Jian Gao, Chun Gu, Youtian Lin, Hao Zhu, Xun Cao, Li Zhang, and Yao Yao. 2023b. Relightable 3d gaussian: Real-time point cloud relighting with brdf decomposition and ray tracing. *arXiv preprint arXiv:2311.16043* (2023).
- William Gao, Noam Aigerman, Thibault Groueix, Vova Kim, and Rana Hanocka. 2023a. Textdeformer: Geometry manipulation using text guidance. In *ACM SIGGRAPH 2023 Conference Proceedings*. 1–11.
- Bingchen Gong, Yuehao Wang, Xiaoguang Han, and Qi Dou. 2023. SeamlessNeRF: Stitching Part NeRFs with Gradient Propagation. In *SIGGRAPH Asia 2023 Conference Papers*. 1–10.
- Benjamin Graham, Martin Engelcke, and Laurens van der Maaten. 2018. 3D Semantic Segmentation with Submanifold Sparse Convolutional Networks. *CVPR* (2018).
- Zekun Hao, Arun Mallya, Serge Belongie, and Ming-Yu Liu. 2021. Gancraft: Unsupervised 3d neural rendering of mincraft worlds. In *Proceedings of the IEEE/CVF International Conference on Computer Vision*. 14072–14082.
- Ayaan Haque, Matthew Tancik, Alexei A Efros, Aleksander Holynski, and Angjoo Kanazawa. 2023. Instruct-nerf2nerf: Editing 3d scenes with instructions. In *Proceedings of the IEEE/CVF International Conference on Computer Vision*. 19740–19750.
- Jonathan Ho, Ajay Jain, and Pieter Abbeel. 2020. Denoising Diffusion Probabilistic Models. In *Advances in Neural Information Processing Systems*, H. Larochelle, M. Ranzato, R. Hadsell, M.F. Balcan, and H. Lin (Eds.), Vol. 33. Curran Associates, Inc., 6840–6851. [https://proceedings.neurips.cc/paper\\_files/paper/2020/file/4c5bfc8584af0d967f1ab10179ca4b-Paper.pdf](https://proceedings.neurips.cc/paper_files/paper/2020/file/4c5bfc8584af0d967f1ab10179ca4b-Paper.pdf)
- Yicong Hong, Kai Zhang, Jiuxiang Gu, Sai Bi, Yang Zhou, Difan Liu, Feng Liu, Kalyan Sunkavalli, Trung Bui, and Hao Tan. 2023. Lrm: Large reconstruction model for single image to 3d. *arXiv preprint arXiv:2311.04400* (2023).
- Emmanuel Iarussi, Adrien Bousseau, and Theophanis Tsandilas. 2013. The drawing assistant: Automated drawing guidance and feedback from photographs. In *ACM Symposium on User Interface Software and Technology (UIST)*. ACM.
- Clément Jambon, Bernhard Kerbl, Georgios Kopanas, Stavros Diolatzis, Thomas Leimkühler, and George Drettakis. 2023. Nerfshop: Interactive editing of neural radiance fields. *Proceedings of the ACM on Computer Graphics and Interactive Techniques* 6, 1 (2023).
- Hyunyoung Jung, Seonghyeon Nam, Nikolaos Sarafianos, Sungjoo Yoo, Alexander Sorkine-Hornung, and Rakesh Ranjan. 2024. Geometry Transfer for Stylizing Radiance Fields. In *Proceedings of the IEEE/CVF Conference on Computer Vision and Pattern Recognition*. 8565–8575.
- Bernhard Kerbl, Georgios Kopanas, Thomas Leimkühler, and George Drettakis. 2023. 3d gaussian splatting for real-time radiance field rendering. *ACM Transactions on Graphics* 42, 4 (2023), 1–14.
- Justin Kerr, Chung Min Kim, Ken Goldberg, Angjoo Kanazawa, and Matthew Tancik. 2023. Lerf: Language embedded radiance fields. In *Proceedings of the IEEE/CVF International Conference on Computer Vision*. 19729–19739.
- Shakiba Kheradmand, Daniel Rebain, Gopal Sharma, Weiwei Sun, Jeff Tseng, Hossam Isack, Abhishek Kar, Andrea Tagliasacchi, and Kwang Moo Yi. 2024. 3D Gaussian Splatting as Markov Chain Monte Carlo. *arXiv preprint arXiv:2404.09591* (2024).
- Chung Min Kim, Mingxuan Wu, Justin Kerr, Ken Goldberg, Matthew Tancik, and Angjoo Kanazawa. 2024. GARField: Group Anything with Radiance Fields. *arXiv preprint arXiv:2401.09419* (2024).

- Sosuke Kobayashi, Eiichi Matsumoto, and Vincent Sitzmann. 2022. Decomposing nerf for editing via feature field distillation. *Advances in Neural Information Processing Systems* 35 (2022), 23311–23330.
- Joo Chan Lee, Daniel Rho, Xiangyu Sun, Jong Hwan Ko, and Eunbyung Park. 2024. Compact 3d gaussian representation for radiance field. In *Proceedings of the IEEE/CVF Conference on Computer Vision and Pattern Recognition*. 21719–21728.
- Weiyu Li, Xuelin Chen, Jue Wang, and Baoquan Chen. 2023. Patch-based 3D natural scene generation from a single example. In *Proceedings of the IEEE/CVF Conference on Computer Vision and Pattern Recognition*. 16762–16772.
- Weiyu Li, Jiarui Liu, Rui Chen, Yixun Liang, Xuelin Chen, Ping Tan, and Xiaoxiao Long. 2024. CraftsMan: High-fidelity Mesh Generation with 3D Native Generation and Interactive Geometry Refiner. *arXiv preprint arXiv:2405.14979* (2024).
- Chen-Hsuan Lin, Jun Gao, Luming Tang, Towaki Takikawa, Xiaohui Zeng, Xun Huang, Karsten Kreis, Sanja Fidler, Ming-Yu Liu, and Tsung-Yi Lin. 2023. Magic3d: High-resolution text-to-3d content creation. In *Proceedings of the IEEE/CVF Conference on Computer Vision and Pattern Recognition*. 300–309.
- Feng-Lin Liu, Hongbo Fu, Yu-Kun Lai, and Lin Gao. 2024. SketchDream: Sketch-based Text-to-3D Generation and Editing. *arXiv preprint arXiv:2405.06461* (2024).
- Ilya Loshchilov and Frank Hutter. 2017. Decoupled weight decay regularization. *arXiv preprint arXiv:1711.05101* (2017).
- Media Molecule. 2020. *Dreams*. <https://indreams.me/>
- Aryan Mikaeli, Or Perel, Mehdi Safaei, Daniel Cohen-Or, and Ali Mahdavi-Amiri. 2023. Sked: Sketch-guided text-based 3d editing. In *Proceedings of the IEEE/CVF International Conference on Computer Vision*. 14607–14619.
- Ben Mildenhall, Pratul P Srinivasan, Matthew Tancik, Jonathan T Barron, Ravi Ramamoorthi, and Ren Ng. 2021. Nerf: Representing scenes as neural radiance fields for view synthesis. *Commun. ACM* 65, 1 (2021), 99–106.
- Mojang Studios. 2011. *Minecraft*. <https://www.minecraft.net/>
- Alexander Mordvintsev, Ettore Randazzo, Eyvind Niklasson, and Michael Levin. 2020. Growing neural cellular automata. *Distill* 5, 2 (2020), e23.
- Jiteng Mu, Michaël Gharbi, Richard Zhang, Eli Shechtman, Nuno Vasconcelos, Xiaolong Wang, and Taesung Park. 2024. Editable Image Elements for Controllable Synthesis. *arXiv preprint arXiv:2404.16029* (2024).
- Thomas Müller, Alex Evans, Christoph Schied, and Alexander Keller. 2022. Instant neural graphics primitives with a multiresolution hash encoding. *ACM transactions on graphics (TOG)* 41, 4 (2022), 1–15.
- Yaniv Nikankin, Niv Haim, and Michal Irani. 2022. Sinfusion: Training diffusion models on a single image or video. *arXiv preprint arXiv:2211.11743* (2022).
- Eyvind Niklasson, Alexander Mordvintsev, Ettore Randazzo, and Michael Levin. 2021. Self-organising textures. *Distill* 6, 2 (2021), e00027–003.
- Oculus VR. 2016. *Oculus Quill*. <https://quill.fb.com>
- Maxime Oquab, Timothée Darcet, Théo Moutakanni, Huy Vo, Marc Szafraniec, Vasil Khalidov, Pierre Fernandez, Daniel Haziza, Francisco Massa, Alaaeldin El-Nouby, et al. 2023. Dinov2: Learning robust visual features without supervision. *arXiv preprint arXiv:2304.07193* (2023).
- Ehsan Pajouheshgar, Yitao Xu, Alexander Mordvintsev, Eyvind Niklasson, Tong Zhang, and Sabine Süsstrunk. 2023. Mesh Neural Cellular Automata. *arXiv preprint arXiv:2311.02820* (2023).
- Panagiotis Papanotakis, Georgios Kopanas, Bernhard Kerbl, Alexandre Lanvin, and George Drettakis. 2024. Reducing the Memory Footprint of 3D Gaussian Splatting. *Proceedings of the ACM on Computer Graphics and Interactive Techniques* 7, 1 (2024), 1–17.
- Ryan Po and Gordon Wetzstein. 2023. Compositional 3d scene generation using locally conditioned diffusion. *arXiv preprint arXiv:2303.12218* (2023).
- Ben Poole, Ajay Jain, Jonathan T Barron, and Ben Mildenhall. 2022. Dreamfusion: Text-to-3d using 2d diffusion. *arXiv preprint arXiv:2209.14988* (2022).
- Alec Radford, Jong Wook Kim, Chris Hallacy, Aditya Ramesh, Gabriel Goh, Sandhini Agarwal, Girish Sastry, Amanda Askell, Pamela Mishkin, Jack Clark, et al. 2021. Learning transferable visual models from natural language supervision. In *International conference on machine learning*. PMLR, 8748–8763.
- Yuchen Rao, Yinyu Nie, and Angela Dai. 2022. Patchcomplete: Learning multi-resolution patches priors for 3d shape completion on unseen categories. *Advances in Neural Information Processing Systems* 35 (2022), 34436–34450.
- Xuanchi Ren, Jiahui Huang, Xiaohui Zeng, Ken Museth, Sanja Fidler, and Francis Williams. 2023. XCube: Large-Scale 3D Generative Modeling using Sparse Voxel Hierarchies. *arXiv preprint arXiv:2312.03806* (2023).
- Daniel Ritchie, Anna Thomas, Pat Hanrahan, and Noah Goodman. 2016. Neurally-guided procedural models: Amortized inference for procedural graphics programs using neural networks. *Advances in neural information processing systems* 29 (2016).
- Robin Rombach, Andreas Blattmann, Dominik Lorenz, Patrick Esser, and Björn Ommer. 2022. High-resolution image synthesis with latent diffusion models. In *Proceedings of the IEEE/CVF conference on computer vision and pattern recognition*. 10684–10695.
- O. Ronneberger, P. Fischer, and T. Brox. 2015. U-Net: Convolutional Networks for Biomedical Image Segmentation. In *Medical Image Computing and Computer-Assisted Intervention (MICCAI) (LNCS, Vol. 9351)*. Springer, 234–241. <http://mb.informatik.uni-freiburg.de/Publications/2015/RFB15a> (available on arXiv:1505.04597 [cs.CV]).
- Paul-Edouard Sarlin, Daniel DeTone, Tomasz Malisiewicz, and Andrew Rabinovich. 2020. Superglue: Learning feature matching with graph neural networks. In *Proceedings of the IEEE/CVF conference on computer vision and pattern recognition*. 4938–4947.
- Vishnu Sarukkai, Linden Li, Arden Ma, Christopher Ré, and Kayvon Fatahalian. 2024a. Collage diffusion. In *Proceedings of the IEEE/CVF Winter Conference on Applications of Computer Vision*. 4208–4217.
- Vishnu Sarukkai, Lu Yuan, Mia Tang, Maneesh Agrawala, and Kayvon Fatahalian. 2024b. Block and Detail: Scaffolding Sketch-to-Image Generation. *arXiv preprint arXiv:2402.18116* (2024).
- Tamar Rott Shaham, Tali Dekel, and Tomer Michaeli. 2019. Singan: Learning a generative model from a single natural image. In *Proceedings of the IEEE/CVF international conference on computer vision*. 4570–4580.
- Nicholas Sharp et al. 2019. Polyscope. [www.polyscope.run](http://www.polyscope.run).
- Janasch Sohl-Dickstein, Eric Weiss, Niru Maheswaranathan, and Surya Ganguli. 2015. Deep unsupervised learning using nonequilibrium thermodynamics. In *International conference on machine learning*. PMLR, 2256–2265.
- Stanislaw Szymanowicz, Christian Rupprecht, and Andrea Vedaldi. 2023. Splatter image: Ultra-fast single-view 3d reconstruction. *arXiv preprint arXiv:2312.13150* (2023).
- Matthew Tancik, Ethan Weber, Evonne Ng, Ruilong Li, Brent Yi, Terrance Wang, Alexander Kristoffersen, Jake Austin, Kamyar Salahi, Abhik Ahuja, et al. 2023. Nerfstudio: A modular framework for neural radiance field development. In *ACM SIGGRAPH 2023 Conference Proceedings*. 1–12.
- Zhenggang Tang, Zhongzheng Ren, Xiaoming Zhao, Bowen Wen, Jonathan Tremblay, Stan Birchfield, and Alexander Schwing. 2024. NeRFDeformer: NeRF Transformation from a Single View via 3D Scene Flows. In *Proceedings of the IEEE/CVF Conference on Computer Vision and Pattern Recognition*. 10293–10303.
- Vadim Tschernezki, Iro Laina, Diane Larlus, and Andrea Vedaldi. 2022. Neural feature fusion fields: 3d distillation of self-supervised 2d image representations. In *2022 International Conference on 3D Vision (3DV)*. IEEE, 443–453.
- Binglun Wang, Niladri Shekhar Dutt, and Niloy J Mitra. 2024a. Proteusnerf: Fast lightweight nerf editing using 3d-aware image context. *Proceedings of the ACM on Computer Graphics and Interactive Techniques* 7, 1 (2024), 1–17.
- Weilun Wang, Jianmin Bao, Wengang Zhou, Dongdong Chen, Dong Chen, Lu Yuan, and Houqiang Li. 2022a. Sindiffusion: Learning a diffusion model from a single natural image. *arXiv preprint arXiv:2211.12445* (2022).
- Yujie Wang, Xuelin Chen, and Baoquan Chen. 2022b. Singrav: Learning a generative radiance volume from a single natural scene. *arXiv preprint arXiv:2210.01202* (2022).
- Zian Wang, Tianchang Shen, Merlin Nimier-David, Nicholas Sharp, Jun Gao, Alexander Keller, Sanja Fidler, Thomas Müller, and Zan Gojic. 2023. Adaptive shells for efficient neural radiance field rendering. *arXiv preprint arXiv:2311.10091* (2023).
- Zhenwei Wang, Tengfei Wang, Gerhard Hancke, Ziwei Liu, and Rynson WH Lau. 2024b. ThemeStation: Generating Theme-Aware 3D Assets from Few Exemplars. *arXiv preprint arXiv:2403.15383* (2024).
- Rundi Wu, Ruoshi Liu, Carl Vondrick, and Changxi Zheng. 2023. Sin3dm: Learning a diffusion model from a single 3d textured shape. *arXiv preprint arXiv:2305.15399* (2023).
- Rundi Wu and Changxi Zheng. 2022. Learning to generate 3d shapes from a single example. *arXiv preprint arXiv:2208.02946* (2022).
- Zhennan Wu, Yang Li, Han Yan, Taizhang Shang, Weixuan Sun, Senbo Wang, Ruikai Cui, Weizhe Liu, Hiroyuki Sato, Hongdong Li, et al. 2024. BlockFusion: Expandable 3D Scene Generation using Latent Tri-plane Extrapolation. *arXiv preprint arXiv:2401.17053* (2024).
- Kevin Xie, Jonathan Lorraine, Tianshi Cao, Jun Gao, James Lucas, Antonio Torralba, Sanja Fidler, and Xiaohui Zeng. 2024a. Latte3d: Large-scale amortized text-to-enhanced3d synthesis. *arXiv preprint arXiv:2403.15385* (2024).
- Tianyi Xie, Zeshun Zong, Yuxing Qiu, Xuan Li, Yutao Feng, Yin Yang, and Chenfanfu Jiang. 2024b. Physgaussian: Physics-integrated 3d gaussians for generative dynamics. In *Proceedings of the IEEE/CVF Conference on Computer Vision and Pattern Recognition*. 4389–4398.
- Jiawei Yang, Boris Ivanovic, Or Litany, Xinshuo Weng, Seung Wook Kim, Boyi Li, Tong Che, Danfei Xu, Sanja Fidler, Marco Pavone, et al. 2023. Emernerf: Emergent spatial-temporal scene decomposition via self-supervision. *arXiv preprint arXiv:2311.02077* (2023).
- Mingqiao Ye, Martin Danelljan, Fisher Yu, and Lei Ke. 2023. Gaussian grouping: Segment and edit anything in 3d scenes. *arXiv preprint arXiv:2312.00732* (2023).
- Vickie Ye, Matias Turkulainen, and the Nerfstudio team. 2024. *gsplat*. <https://github.com/nerfstudio-project/gsplat>
- Yu-Jie Yuan, Yang-Tian Sun, Yu-Kun Lai, Yuewen Ma, Rongfei Jia, and Lin Gao. 2022. Nerf-editing: geometry editing of neural radiance fields. In *Proceedings of the IEEE/CVF Conference on Computer Vision and Pattern Recognition*. 18353–18364.
- Dongsu Zhang, Changwoon Choi, Jeonghwan Kim, and Young Min Kim. 2021. Learning to generate 3d shapes with generative cellular automata. *arXiv preprint arXiv:2103.04130* (2021).
- Dongsu Zhang, Changwoon Choi, Inbum Park, and Young Min Kim. 2022. Probabilistic implicit scene completion. *arXiv preprint arXiv:2204.01264* (2022).

- Deheng Zhang, Clara Fernandez-Labrador, and Christopher Schroers. 2024. Coarf: Controllable 3d artistic style transfer for radiance fields. *arXiv preprint arXiv:2404.14967* (2024).
- Lvmin Zhang, Anyi Rao, and Maneesh Agrawala. 2023. Adding conditional control to text-to-image diffusion models. In *Proceedings of the IEEE/CVF International Conference on Computer Vision*. 3836–3847.
- Wanguandong Zheng, Haifeng Xia, Rui Chen, Ming Shao, Siyu Xia, and Zhengming Ding. 2024. Sketch3D: Style-Consistent Guidance for Sketch-to-3D Generation. *arXiv preprint arXiv:2404.01843* (2024).
- Shijie Zhou, Haoran Chang, Sicheng Jiang, Zhiwen Fan, Zehao Zhu, Dejia Xu, Pradyumna Chari, Suyu You, Zhangyang Wang, and Achuta Kadambi. 2023. Feature 3dgs: Supercharging 3d gaussian splatting to enable distilled feature fields. *arXiv preprint arXiv:2312.03203* (2023).
- Jingyu Zhuang, Chen Wang, Liang Lin, Lingjie Liu, and Guanbin Li. 2023. Dreameditor: Text-driven 3d scene editing with neural fields. In *SIGGRAPH Asia 2023 Conference Papers*. 1–10.

## A TRAINING GENERATIVE CELLULAR AUTOMATA

### A.1 Infusion Training and Loss

GCA is trained through a process called *Infusion* [Bordes et al. 2017]. Intuitively, starting from a state  $s^0$ , *Infusion* supervises the learned transition kernel  $p_\theta(s^{t+1}|s^t)$  to stay close to an “infused kernel” biased towards a target shape  $x$ :

$$q_\theta^t(s^{t+1}|s^t, x) = \prod_{c \in \mathcal{N}(s^t)} q_\theta^t(o_c, z_c|s^t, x) \quad (10)$$

$$= \prod_{c \in \mathcal{N}(s^t)} q_\theta^t(o_c|s^t, x) q_\theta^t(z_c|s^t, o_c, x), \quad (11)$$

which is factorized similar to the transition kernel in Equations 3 and 4. The conditional distributions of  $o_c$  and  $z_c$  are gradually biased towards the ground truth final shape  $x$  according to an infusion rate  $\alpha^t$  which increases linearly with time step  $t$ , i.e.,  $\alpha^t = \min(\alpha_1 t + \alpha_0, 1)$ , where  $\alpha_1 > 0$ :

$$q_\theta^t(o_c|s^t, x) = \text{Ber}((1 - \alpha^t)\lambda_{\theta,c} + \alpha^t \mathbf{1}[c \in x]), \quad (12)$$

$$q_\theta^t(z_c|s^t, o_c, x) = \begin{cases} \delta_0 & \text{if } o_c = 0 \\ N((1 - \alpha^t)\mu_{\theta,c} + \alpha^t z_c^x, \sigma^t \mathbf{I}) & \text{if } o_c = 1. \end{cases} \quad (13)$$

where  $\mathbf{1}$  designates the indicator function and  $\mathbf{I}$  the identity matrix.

To learn to generate  $x \sim s^T$  from an initial state  $s^0$ , intermediate states  $s^{1:T}$  are recursively sampled from the infused kernel  $q_\theta(s^{t+1}|s^t, x)$ . For each sampled state  $s^t$ , GCA is trained by minimizing the loss  $\mathcal{L}_t$  defined as the KL divergence between the infused kernel and the transition kernel [Zhang et al. 2022], which following the factorization defined in Equation 11 can be decomposed into:

$$\begin{aligned} \mathcal{L}_t &= D_{KL}(q_\theta(o_c, z_c) \| p_\theta(o_c, z_c)) \\ &= \sum_{c \in \mathcal{N}(s^t)} \underbrace{D_{KL}(q_\theta(o_c|s^t, x) \| p_\theta(o_c|s^t))}_{\mathcal{L}_o} \\ &\quad + \underbrace{q_\theta(o_c = 1|s^t, x) D_{KL}(q_\theta(z_c|s^t, x, o_c = 1) \| p_\theta(z_c|s^t, o_c = 1))}_{\mathcal{L}_z}. \end{aligned} \quad (14)$$

Since  $\mathcal{L}_o$  and  $\mathcal{L}_z$  are the KL divergence between Bernoulli and normal distributions, respectively,  $\mathcal{L}_t$  can be derived in closed-form. In practice, the scale of  $\mathcal{L}_z$  is much larger than that of  $\mathcal{L}_o$  and  $\mathcal{L}_z$  is down-weighted by a factor  $\lambda_z$ . We follow Zhang et al. [2022] and use  $\lambda_z = 0.01$ .

### A.2 Discussion on GCA Training

While experimenting with GCA for single-exemplar training, we realized two main caveats of the loss defined by Equation 14.

*Invalid variation lower bound.* In Zhang et al. [2022],  $\mathcal{L}_t$  is derived through the evidence lower bound. In what follows, we show that this holds but the corresponding proposal distribution is intractable and not the one used during training. Let  $x$  be the target exemplar shape, we can bound the log-likelihood as follows:

$$\begin{aligned} \log p_\theta(x) & \quad (15) \\ & \geq \mathbb{E}_{q_\theta(s^{0:T-1}|x)} \left[ \log \frac{p_\theta(s^{0:T-1}, x)}{q_\theta(s^{0:T-1}|x)} \right] \quad (16) \\ & = \mathbb{E}_{q_\theta(s^{0:T-1}|x)} \left[ \log \frac{p(s^0)}{q(s^0)} \right] + \mathbb{E}_{q_\theta(s^{0:T-1}|x)} \left[ \sum_{t=0}^{T-2} \log \frac{p_\theta(s^{t+1}|s^t)}{q_\theta(s^{t+1}|s^t, x)} \right] \\ & \quad + \mathbb{E}_{q_\theta(s^{0:T-1}|x)} \left[ \log p(x|s^{T-1}) \right] \quad (17) \\ & = \underbrace{\mathbb{E}_{q_\theta(s^0|x)} \left[ \log \frac{p(s^0)}{q(s^0)} \right]}_{(a)} + \sum_{t=0}^{T-2} \underbrace{\mathbb{E}_{q_\theta(s^t, s^{t+1}|x)} \left[ \log \frac{p_\theta(s^{t+1}|s^t)}{q_\theta(s^{t+1}|s^t, x)} \right]}_{(b)} \\ & \quad + \underbrace{\mathbb{E}_{q_\theta(s^{T-1}|x)} \left[ \log p(x|s^{T-1}) \right]}_{(c)} \quad (18) \end{aligned}$$

where Equation 16 is obtained with Jensen’s inequality, Equation 17 from the factorized state transitions and Equation 18 by the assumption of independence between states.

In Equation 18, (a) is constant with the definition of  $q_\theta$  and we ignore (c) in the discussion that follows. If we focus on (b) for an arbitrary  $t$ , we see that it can be rewritten according to Equation 20.

$$\begin{aligned} (b) &= \mathbb{E}_{q_\theta(s^t|x)} \left[ \sum_{s^{t+1} \in \mathcal{S}} q_\theta(s^{t+1}|s^t, x) \log \frac{p_\theta(s^{t+1}|s^t)}{q_\theta(s^{t+1}|s^t, x)} \right] \quad (19) \\ &= -\mathbb{E}_{q_\theta(s^t|x)} \left[ D_{KL}(q_\theta(s^{t+1}|s^t, x) \| p_\theta(s^{t+1}|s^t)) \right] \quad (20) \end{aligned}$$

This is consistent with the loss term in Equation 14. However, contrary to the proof given by Zhang et al. [2022], our expectation is rigorously derived. The problem with this expectation lies in the fact that  $q_\theta(s^t|x)$  is intractable. In the formalism of diffusion models, an analogous derivation would be solved by using the reversal of the diffusion process. Unfortunately, in the case of infusion, there is no closed-form forward process from the complete shape  $x$  to  $s^t$ . Furthermore, the way samples are drawn when applying loss  $\mathcal{L}_t$  does not follow the distribution over which the conditional expectation is taken, namely  $q_\theta(s^t|x)$ . Nevertheless, this loss remains intuitively consistent as it guides the optimized distribution to a target distribution, a scheme that has been proposed in previous works [Ritchie et al. 2016].

*Degeneracy of the loss.* As training progresses the distribution modeled by  $p_\theta(o_c, z_c)$  gets closer to  $q_\theta(o_c, z_c)$ . However,  $q_\theta(o_c, z_c)$  depends directly on  $\theta$  as it is a mixture of the latter and the exemplar as defined in Equation 12 and Equation 13. When training with a single exemplar, this distribution is very narrow and thus causes



Fig. 17. In this figure, we generate voxels hierarchically using our sparse patch-based optimization strategy. The coarsest resolution  $r_c = 16^3$  is initialized with the conditioning voxels (row 1) and random features. For each resolution, we apply the same parameters as introduced in Section 5.3 and we upsample each resolution by a factor of 2. This approach leads to repetitive patterns, lacks spatial and semantic consistency (columns 1-2), and inflates geometry beyond the conditioning input. To highlight the latter point, we voluntarily overlaid the generated result on the conditioning input at scale.

the loss to be unstable as training converges. This phenomenon is exacerbated considering that GCA uses a single network  $p_\theta$  agnostic of the value of  $t$  to model state transitions. This is in stark contrast to diffusion models for which  $t$  is given as an additional parameter to the denoising network [Ho et al. 2020; Sohl-Dickstein et al. 2015]. In the case of GCA, this is however not conceivable as there is no fixed “forward process”. In other words, the proposal distribution  $q_\theta$  is both data-dependent and changes during training because it depends directly on the transition kernel  $p_\theta$  that is being optimized. It is also worth noting that, for the same reason, there is no way to control variance in a principled manner in contrast to diffusion models for which the forward process is fixed. Furthermore, using Bernoulli transition kernels to model occupancy precludes simultaneous control over both mean and variance at the same time.

To mitigate these issues, we observed that it is crucial to train GCA with as few steps as necessary to reach the target distribution. As suggested by the original *Infusion* work [Bordes et al. 2017], it is possible to sample more steps at inference than used during training. For our conditional generation task analogous to a form of completion, we thus choose  $T = 5$  during training and  $T = 7$  for generation.

## B KEY DIFFERENCES WITH SIN3DGEN

In what follows we highlight the key differences between our patch consistency step introduced in Section 5.3 and the patch-based synthesis algorithm proposed by Sin3DGen [Li et al. 2023].

*Consistency step & controllable generation.* We target a different application than Sin3DGen, namely enforcing consistency on the prediction of GCA as shown in Figure 8. As a consequence, we use

patch-based optimization at a single resolution (i.e., target resolution  $r_t$ ) while the latter generates patches in a hierarchical manner thus focusing on reproducing multi-scale patch statistics. By offloading the controllable generation task to GCA, we ensure explicit control over generated objects, even for semantically structured objects. To perform editing, Sin3DGen [Li et al. 2023] initializes coarser levels with a geometric proxy, analogous to our coarse conditioning voxels, and subsequently synthesizes finer levels from this initialization. In Figure 17, using the same exemplars as Figure 9, we show that adapting this hierarchical patch-based synthesis strategy to our sparse formulation fails to respect the initial conditioning constraints, cannot handle semantically complex distributions and leads to repetitive patterns.

*Sparse formulation.* Even though Sin3DGen starts from Plenoxels [Fridovich-Keil et al. 2022], a sparse representation of a radiance field, it still synthesizes patches in a *dense* manner. This is key to being able to propagate geometric changes during generation. As it is prohibitively expensive, the process is made tractable by using *approximate* matching with a *Nearest-Neighbor Field* (NNF) introduced in *PatchMatch* [Barnes et al. 2009]. On the other hand, we assume that geometry is already solved by the GCA and we are only interested in minor refinements. Furthermore, we seek a formulation that can map directly to (a) the output of GCA, namely sparse voxels with features, and (b) the explicit nature of the 3D Gaussians we use to model appearance (we do not model a radiance field that can easily be converted to signed distance function values). Note also that by keeping a sparse representation, we can match patches exhaustively without approximations. This choice entails designing a proper distance function and a way to update geometry locally (voting mechanism).

*Distance choice & voting mechanism.* In essence, our matching distance is inspired by Sin3DGen as it balances geometry and feature consistency. However, we represent occupancy explicitly as a binary variable  $O_i$  and not a signed distance value, and we compare features using cosine similarity instead of L2 norm. As our features are renormalized (i.e., unit norm) and empty voxels in a patch are given zero features, this allows us only to compare only features for which occupancy is matched. Similarly to Sin3DGen, our features are based on PCA-ed spherical harmonics but we additionally introduce guidance from semantic features, namely PCA-ed DINO features. As we rely on a sparse representation, we cannot update and propagate geometry through a continuous signed distance field. To this extent, our voting mechanism allows us to *refine* geometry locally.

## C ADDITIONAL IMPLEMENTATION DETAILS

### C.1 3D Gaussian Splatting

Our implementation of 3D Gaussian Splatting is based on a standalone re-implementation of the *splatfacto* model in *nerfstudio* [Tancik et al. 2023]. It uses *gsplat* v.0.1.11 for differentiable rendering routines. We use the default parameters of the *splatfacto* model with a few exceptions. To avoid large 3D Gaussians, we use the scale regularization of PhysGaussian [Xie et al. 2024b] with a maximum Poisson ratio of 10.0. When pre-processing primitives, we clip the



scale of 3D Gaussians so that their scale does not exceed twice the size of a voxel at the target voxel resolution  $r_t$ .

Our datasets were processed with COLMAP through *nerfstudio*. For challenging datasets, we used *Superpoint* descriptors [DeTone et al. 2018] and *SuperGlue* [Sarlin et al. 2020] for matching. To extract DINO features, we relied on the implementation of EmerNeRF [Yang et al. 2023].

When applying affine transformation to 3D Gaussians during editing, we properly transform their mean, scale, and rotation components. Additionally, we rotate spherical harmonics as Gaussians often “bake” appearance into view-dependent effects.

## C.2 Generative Cellular Automata

Our implementation of Generative Cellular Automata is based on the original codebase of Zhang et al. [2021, 2022]. However, we introduce a number of key modifications that we describe in this section.

We use the standard neighborhood over the generalized one  $G_X(s^t)$  introduced in cGCA [Zhang et al. 2022]. The reason is that our task can be seen as an inpainting task, where connectivity is ensured due to our choice of initialization:  $s^0$  is obtained by down-sampling the coarse conditioning voxels from resolution  $r_c$  to  $r_t$ . In practice, we use a neighborhood of size 2 w.r.t. L1 distance for our transition kernel. Our infusion schedule follows Zhang et al. [2021, 2022] and grows linearly from  $\alpha_0 = 0.1$  to  $\alpha_T = 0.25$ . Similarly,  $\sigma_t$  follows  $\sigma_t = e^{-1-0.01t}$ .

To mitigate the degeneracy of the KL loss described in Appendix A.2 and considering that we can see the task of the GCA as an infilling task starting from the upsampled coarse conditioning voxels, we use a low value for  $T$ . In practice, we choose  $T = 5$  during training. At inference, we use  $T = 7$  as it allows the GCA to self-correct itself for a couple of additional steps. We additionally perform one mode-seeking step as proposed by Zhang et al. [2022].

Our shallow “U-Net Light” is based on the template of Dhariwal and Nichol [2021] where the number of residual blocks is set to 1 and initial channels to 16. Note that as we discussed previously, we don’t condition the network on  $t$ . We use batch normalization instead of group normalization and ReLU activation instead of SiLU. We noticed that the implementation of Zhang et al. [2022] does not input  $o_c$  to  $p_\theta$ . We restored it as it breaks the formulation introduced in Section 5.1. We use *AdamW* [Loshchilov and Hutter 2017] with a learning rate of  $5 \times 10^{-4}$  and weight decay of  $1 \times 10^{-6}$ . We train for only 10000 iterations as convergence is reached quickly and longer training leads to overfitting due to the limited capacity of our model and data scarcity. We removed most implementation-level performance bottlenecks by batching every possible operation. Note that training and inference speed could certainly be improved with more advanced sparse tensor libraries and support for half-precision. We leave this for future works.

## D ADDITIONAL FIGURES

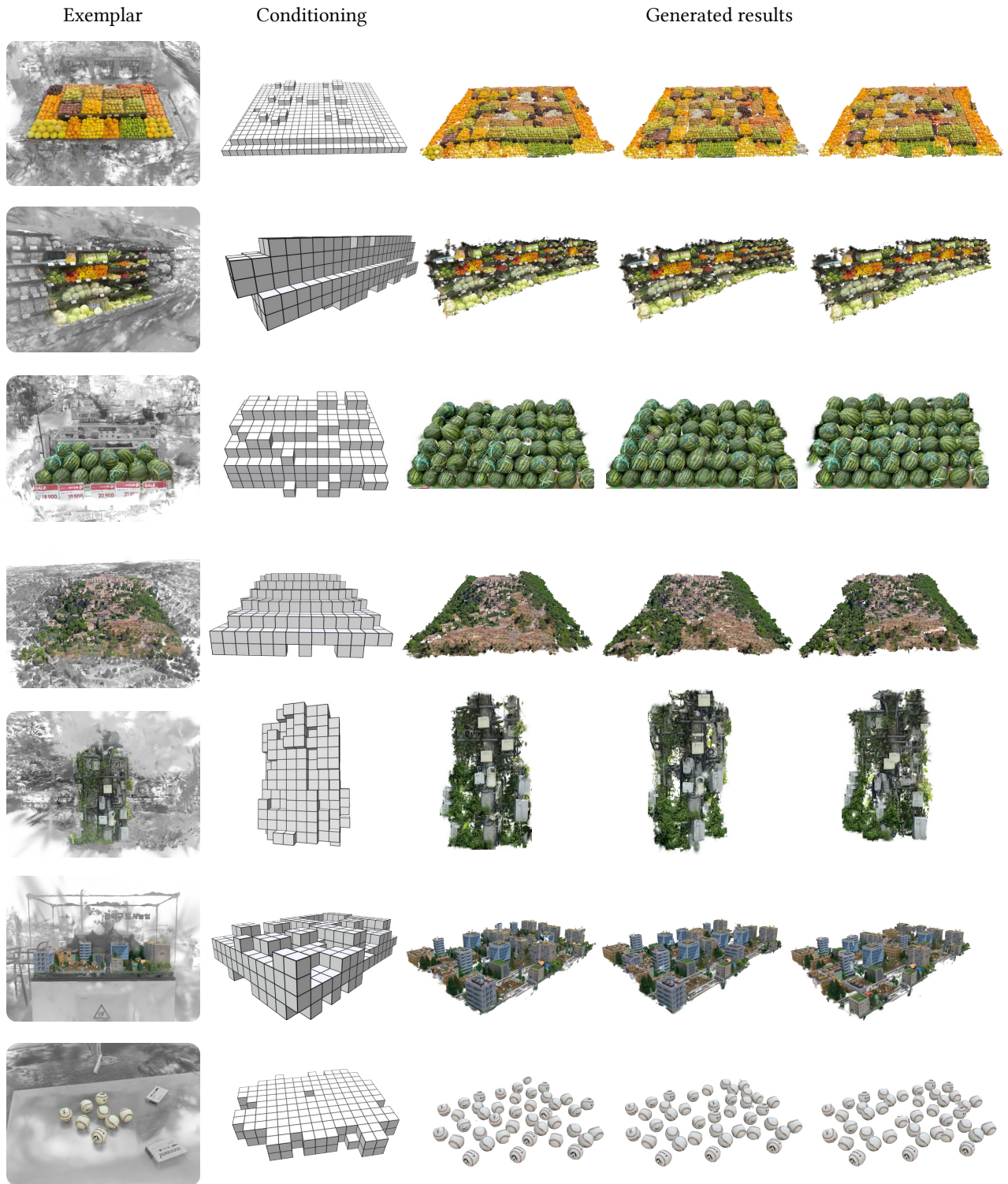


Fig. 18. From a single exemplar, our primitives can generate diverse results given a coarse conditioning signal. Generation can be performed and visualized within 0.5-2 seconds in the editor allowing the user to refine the conditioning input to generate a target asset iteratively.

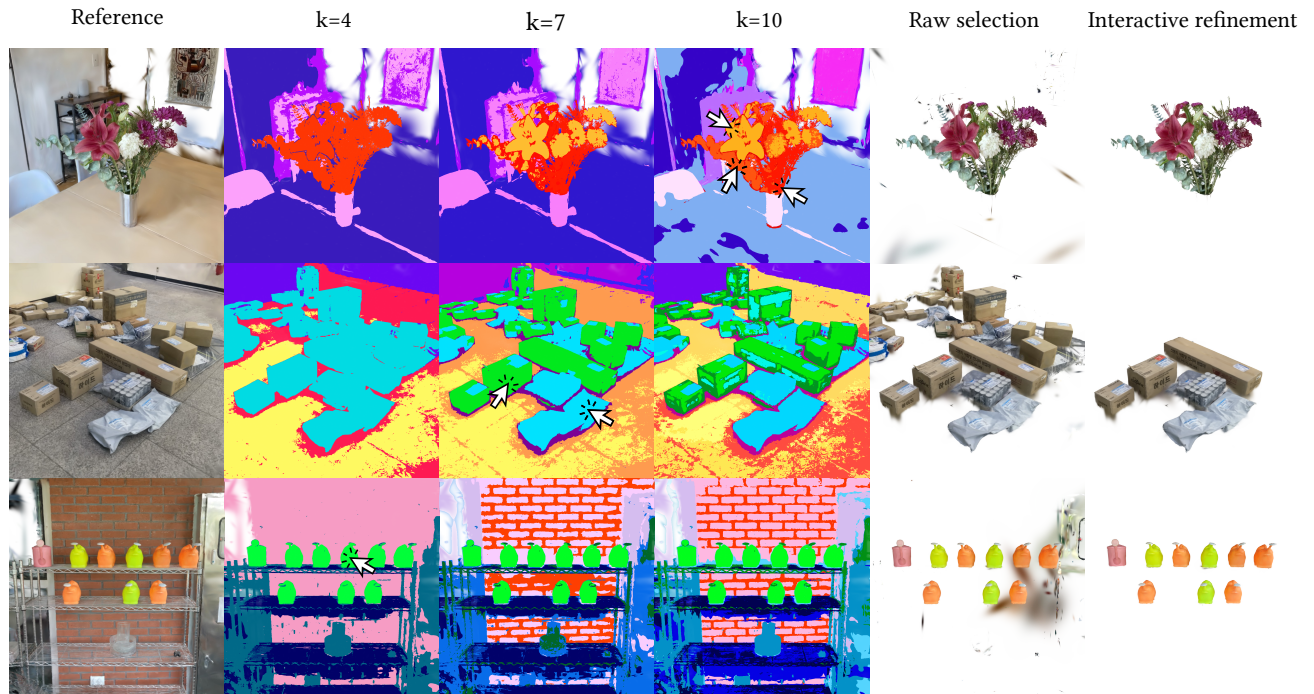


Fig. 19. In addition to view-dependent color, we distill low-dimensional view-independent features  $f$ , namely PCA-ed DINO features. When clustered and rendered, these features provide semantic segments that can be used to select regions within the scene. In columns 2 to 4, we show the segments that are instantly exposed to the user for different values of  $k$ . Upon selection, the corresponding 3D Gaussians can be isolated (column 5). In column 6, we show that additional refinements can be performed using an interactive 3D selection tool shown at the bottom of Figure 3.a and in the supplemental video.

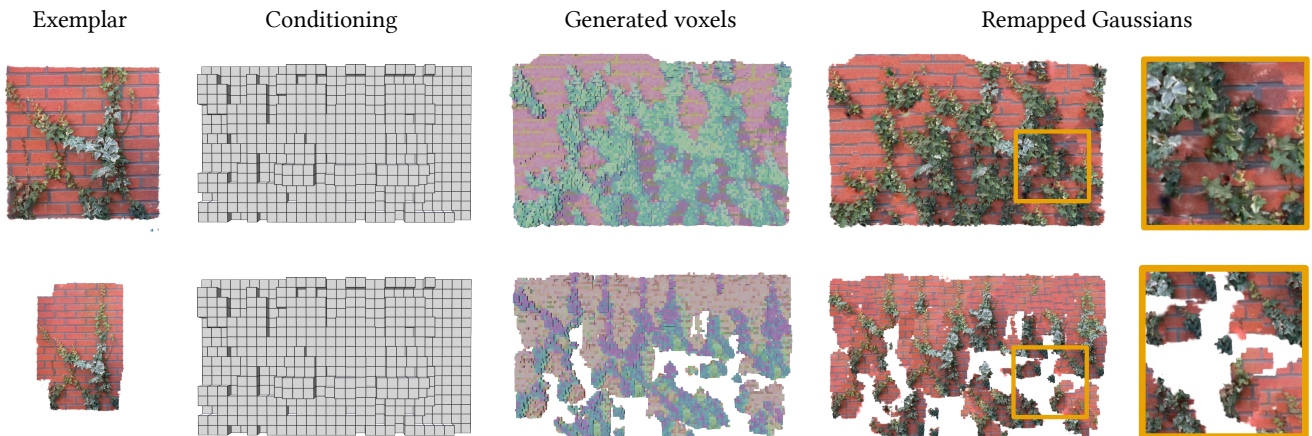


Fig. 20. In this figure, we start from one scene and perform two different selections (left-most column). The first row shows a well-defined crop of the wall with a square shape, whereas the second row shows a more irregular selection. The irregular selection results in severe missing parts for both the GCA-generated voxels and the corresponding remapped Gaussians after the patch consistency step, as the primitives try to reproduce spurious corners included at the selection boundaries.

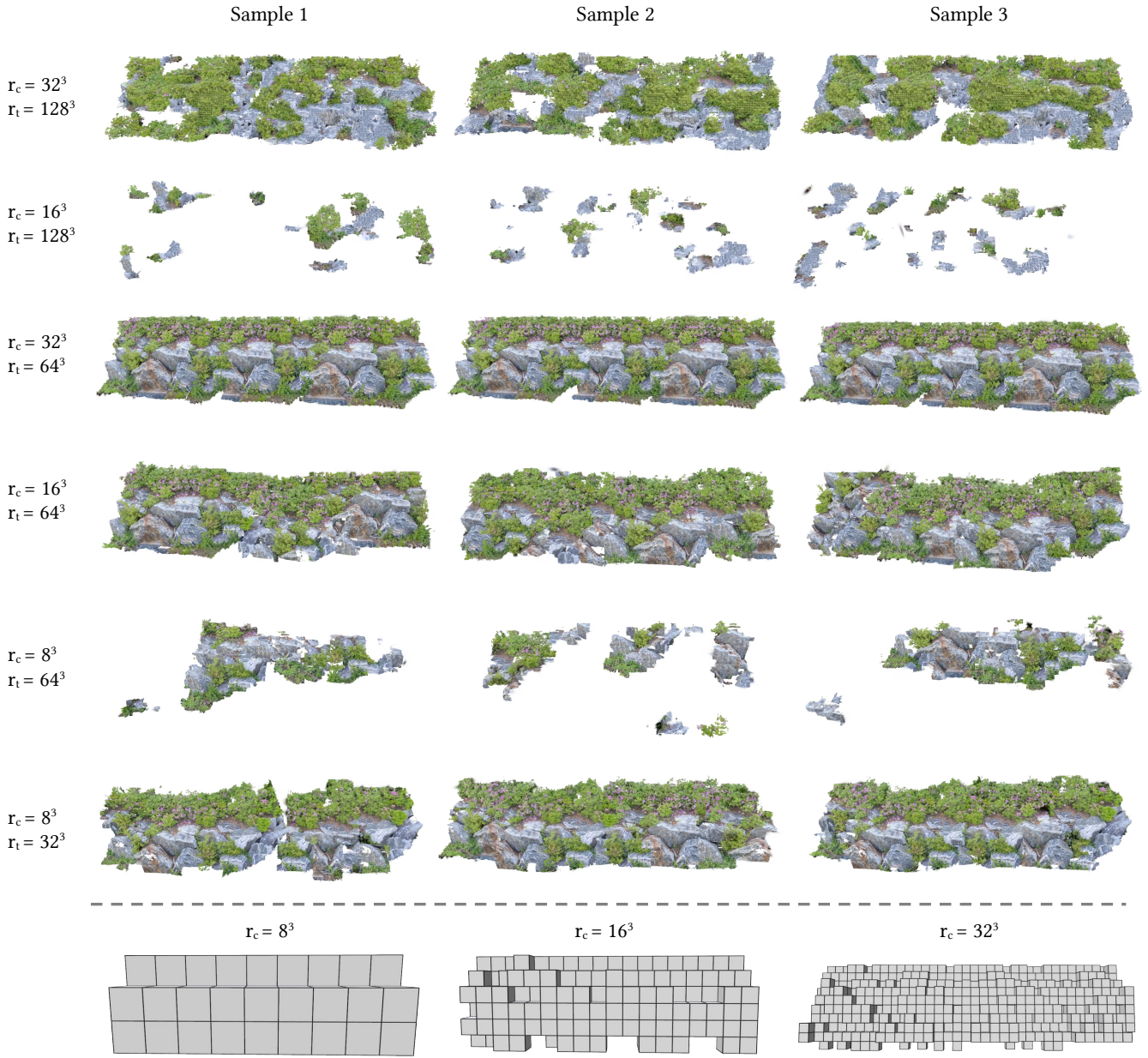


Fig. 21. Illustration of the impact of the target resolution  $r_t$  and conditioning resolution  $r_c$ . The first row shows that generating at a very fine resolution (i.e.,  $r_t = 128^3$ ) causes the GCA to focus on higher-frequency details and miss structure. Conversely, a coarse target resolution (i.e.,  $r_t = 32^3$ ) results in "blocky" outputs. The relative scales between the conditioning and the target are crucial to balance fidelity and diversity. If the difference is too high, GCA fails to recover the shape. This is due to our choice of neighborhood and the conditioning mechanism introduced in Section 5.2. Conversely, conditioning at a resolution too close to the target one (middle row) results in complete overfitting on the exemplar.

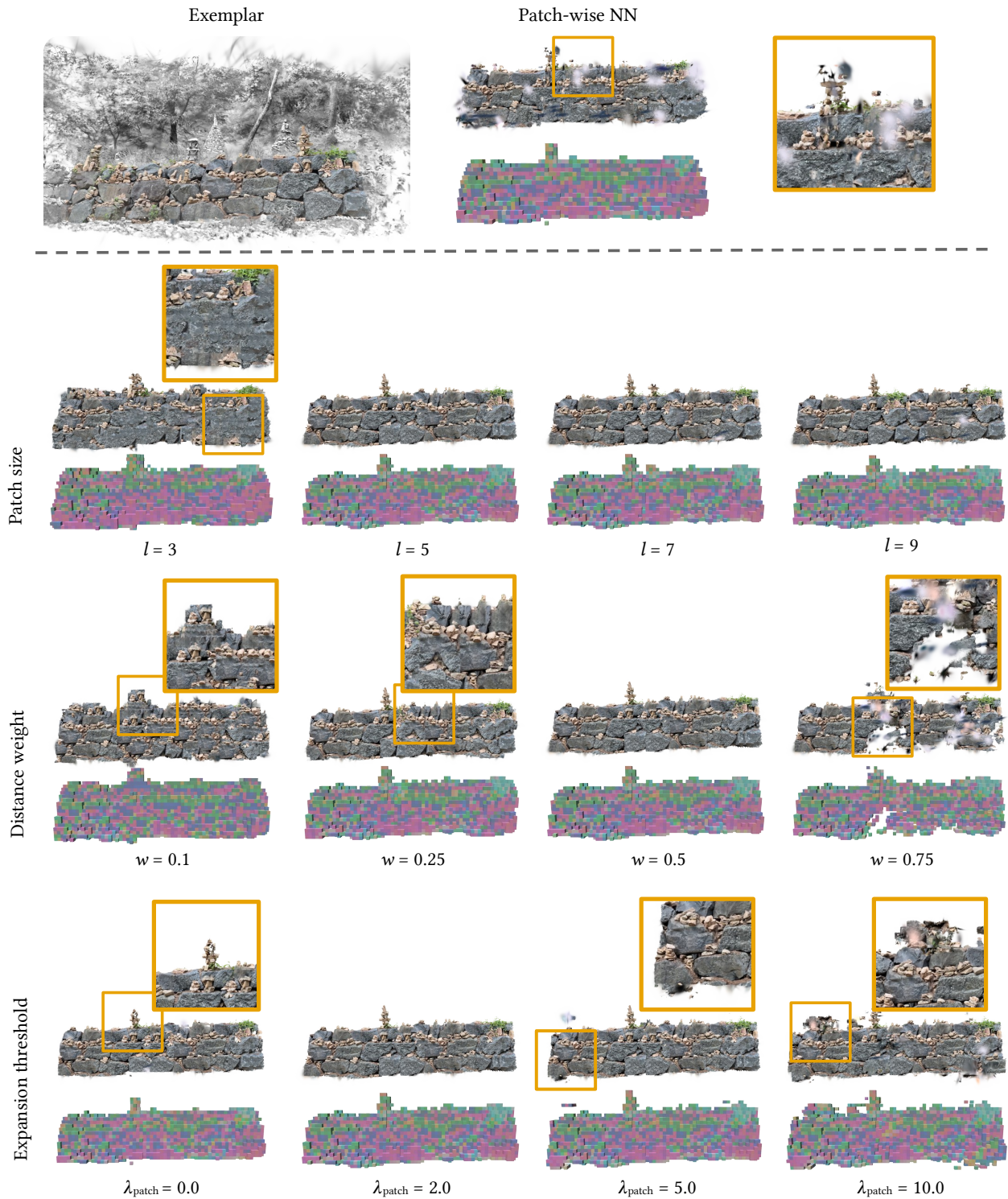


Fig. 22. Impact of the different parameters of our sparse patch consistency algorithm. For each parameter, we start from our default configuration, namely  $l=5$ ,  $w=0.5$ , and  $\lambda_{\text{patch}}=2$ , and vary the parameter of interest. Patch size side-length  $l$  trades local statistics off for larger ones at the cost of increased computations. Distance weight  $w$  balances occupancy matching with patch-wise feature matching. Maximum expansion distance  $\lambda_{\text{patch}}$  enables geometric corrections but leads to artifacts when set too high.